PATCH ANTENNA CHARACTERIZATION IN A HIGH-VOLTAGE CORONA PLASMA

A Thesis
Presented to
The Academic Faculty

by

Marcin M. Morys

In Partial Fulfillment
of the Requirements for the Degree
Master of Science in the
School of Electrical and Computer Engineering

Georgia Institute of Technology
December 2013

PATCH ANTENNA CHARACTERIZATION IN A HIGH-VOLTAGE CORONA PLASMA

Approved by:

Professor Gregory D. Durgin, Advisor
School of Electrical and Computer Engineering
Georgia Institute of Technology

Professor Andrew F. Peterson
School of Electrical and Computer Engineering
Georgia Institute of Technology

Professor Paul G. Steffes
School of Electrical and Computer Engineering
Georgia Institute of Technology

Date Approved: 4 November 2013

To my parents,

Marian and Jolanta.

ACKNOWLEDGEMENTS

I want to thank my committee for taking the time to review my thesis. To my advisor, Gregory Durgin, I extend great appreciation for guiding me in my search for new questions. Mom and dad, thank you for always showing me your support, never demanding anything in return. To my siblings, Anna, Adam, and Monica, thanks for all the fun along the way. Last but not least, a great thank you to all my fellow researchers in the Propagation Group, Chris, Blake, Bashir, and Francesco, for your insights and ideas always freely given.

TABLE OF CONTENTS

LIST OF TABLES

LIST OF FIGURES

SUMMARY

In order to improve efficiency and reliability of the world's power grids, sensors are being deployed for constant status monitoring. Placing inexpensive wireless sensors on high-voltage power lines presents a new challenge to the RF engineer. Large electric field intensities can exist around a wireless sensor antenna on a high-voltage power line, leading to the formation of a corona plasma. A corona plasma is a partially ionized volume of air formed through energetic electron-molecule collisions mediated by a strong electric field. This corona can contain large densities of free electrons which act as a conducting medium, absorbing RF energy and detuning the sensor's antenna.

Through the use of low-profile antennas and rounded geometries, the possibility for corona formation on the antenna surface is greatly reduced, as compared with wire antennas. This study looks at the effects of a corona plasma on a patch antenna, which could be used in a power line sensor. The corona's behavior in the presence of an electromagnetic plane wave is analyzed mathematically to understand the dependence of attenuation on frequency and electron density. A Drude model is used to convert plasma parameters such as electron density and collision frequency to a complex permittivity that can be incorporated in antenna simulations.

Using CST Microwave Studio, a $5.8GHz$ patch antenna is simulated with a plasma material on its surface, of varying densities and thicknesses. Power absorption by the plasma dominates the power loss, as opposed to detuning. A wideband patch is simulated to show that the detuning effects by the plasma can be further reduced. Power absorption by the plasma is significant for electron densities greater than $10^{18}m^{-3}$. However, small point corona are found to have little effect on antenna radiation.

CHAPTER I

INTRODUCTION

1.1 High-Voltage Power Distribution

Electrical power is an integral part of our everyday lives. There are over 18,000 electrical generators in the United States capable of producing over 1 TW of total power [2]. The power from these plants must be distributed to over 300 million residents along with an equally impressive number of businesses and facilities. In order to achieve the massive distribution of power over 3 million square miles of land area, the electrical grid employs approximately 170,000 miles of high-voltage power transmission lines which operate over 100 kV.

With the push for introducing more "green" sources of power, i.e. power generators with little-to-no carbon byproducts, the number of wind turbines and solar panel farms is growing [3]. The difficulty in introducing these power sources into the grid is their inherent output instability due to changing winds or solar intensity. The constantly varying load on the grid due to usage fluctuations must also be monitored in order to supply power where it is needed. In order to maximize the efficiency of power distribution, constant monitoring and corrective measures must be applied.

The constant monitoring of the current, temperature, etc. of a power line itself poses a great problem. The measurement of current is commonly accomplished by a simple step down transformer on the line. A major issue is transmitting the measured information to the ground where it can be processed or forwarded to a central monitoring station. The sensing device, such as a transformer, is on the line, and as such at a high potential, often in the tens or hundreds of kilovolts AC. AC here refers to alternating current, with a frequency of 50-60 Hz. The receiver is located somewhere

on the ground at ground potential. Transmitting information from a high potential to low potential without a physical connection that could provide a pathway for current flow presents a problem.

In modern information transmission systems, a basic conduit for information transmission is a conductive wire. Some modulated voltage at one end of the wire propagates to the other end where the information is received. In the further discussion here, the high-voltage power line will be referred to as the power line, and the information carrying line between the sensor and the ground will be referred to as the transmission line.

Using a conductive medium such as a wire for information transmission from the sensor at high potential to the reader at ground potential provides a low resistance path between the two points. This can be extremely dangerous. A short-circuit between the power line and the ground would send enough current through the transmission line to destroy it, the sensor, or, even damage the power line itself. Nevertheless, such systems are utilized to a great extent. A current sensor in such a system consists of a current transformer which is often immersed in oil for cooling and insulating purposes. The power line passes through an oil-filled container which is insulated from ground with a ceramic bushing. Inside the container is a secondary sensing coil connected to ground with a wire passing through the ceramic bushing. The sharpest potential drop from the power line to ground exists in the oil between the power line and sensing coil. A diagram of a high-voltage current transformer measurement system is shown in Figure 1.

The oil is used as an insulator between the current sensing coil and the power line in part because of its high resistivity and dielectric strength. Another function of the oil is for cooling, especially in power transformers. The term dielectric strength, which will be discussed in a subsequent section, is used to refer to the uniform electric field intensity necessary to ionize a material. If the potential gradient between two objects

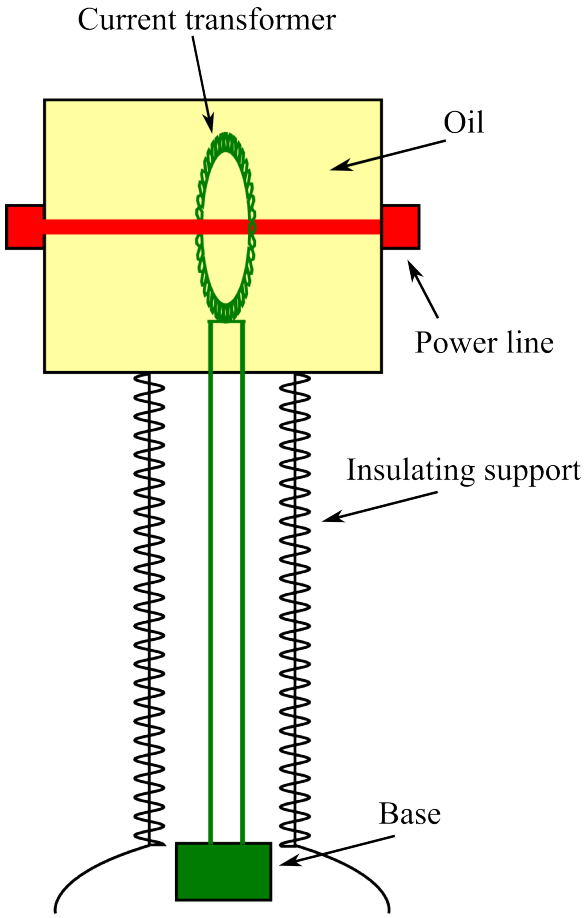

Figure 1: Basic diagram of a current transformer sensor. The red is the power line at high potential, green are the sensing lines at ground potential, and yellow is the insulating oil.

is larger than the dielectric strength of the insulating material separating them, the insulator may break down creating a highly conductive path of free electrons known as an arc. An arc is in essence a short between the two potentials, and poses a hazard. Since the oil has a high dielectric strength, a larger potential gradient is needed to cause breakdown. This means there can be a higher potential difference between the power line and sensing coil, or they can be put closer together than in a system where the insulator has a low dielectric strength. Air has a typical dielectric strength of 30 kV/cm, while transformer oil has a dielectric strength on the order of 100 to 400 kV/cm. Given the operating constraints of high-voltage current transformers as described, these devices can be expensive and bulky. Their installation is also practically limited to power substations where power lines pass close to the ground. As such, they are not conducive to use in a large scale distribution of sensors as required by a smart grid.

Another solution to the distributed sensing problem is the use of remote sensing. By placing a sensitive and well calibrated field sensor, such as a coil or resistive wire, beyond the power line, the electromagnetic fields generated by the power line can be detected and correlated to the status of the line without the need for bulky insulators. The large distance between the sensor and power line provides an airgap for electrical insulation. A difficulty in implementing this method is the field distortion by nearby objects, such as trees. Also, in three-phase power transmission there are three power lines running parallel to one another. A remote sensing coil could register changes in current on the other lines, leading to ambiguity in the measured values. This is especially true in the critical cases where unwanted transients might appear on a line. A more detailed discussion of power line sensing technologies can be found in [4],[5].

A developing solution to the problem of high-voltage sensing is wireless communication. Using a wireless link eliminates the need for a physical connection between the power line and ground. The air gap provides sufficient separation to act as an

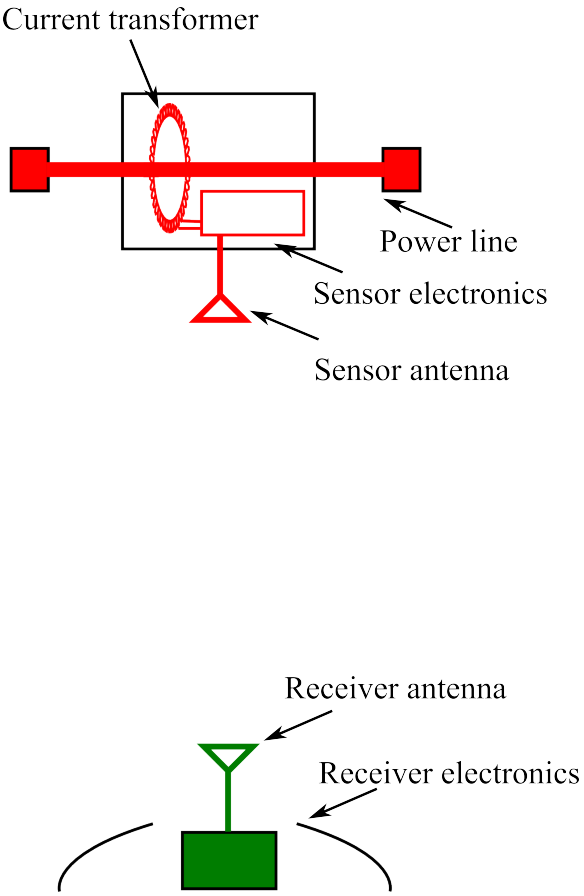

Figure 2: Basic diagram of a wireless current transformer sensor. The red is the power line and sensor at high potential and green is the receiver at ground potential. The sensor must now include circuitry for encoding the information about the current and transmitting it to the receiver.

insulator. Since the sensing coil is no longer physically connected to ground, it can be placed directly on the power line at line potential. Eliminating the oil insulation container reduces size and installation complexity in the design.

When implementing a wireless power line monitoring system, one faces certain challenges. In order to understand these issues, Figure 2 illustrates a basic wireless sensor setup. This basic setup involves a transmitter on the power line and a receiver on the ground. The transmitter must be able to send the power line sensor information to the receiver reliably and accurately. In order to maximize the accuracy of the received data and lower power requirements, a digital encoding scheme should be

implemented. To ensure a reliable communication link between the transmitter and receiver, the two systems must each have a constant source of power, and the communication channel must be understood to mitigate missed or dropped information packets [6]. A packet here refers to a single "chunk" of information that is encoded digitally and transmitted.

As seen in Figure 2, a sensor such as a current transformer is placed directly on the power line. The relative ground potential for the tag electronics is the power line potential. The sensor's electronics digitally sample the sensor information, whether it be line voltage, current, temperature, etc. A radio frequency (RF) carrier frequency is generated and modulated with the digitally encoded sensor data and transmitted to the receiver. The receiver can then demodulate and decode the data to extract the senor information for analysis or further relay.

Harvesting small amounts of power directly from the power line is a simple and viable option for powering the sensor electronics. Energy harvesting is a technique whereby power from an external source is collected, often in the form of an alternating current, rectified to a direct current (DC) voltage, and utilized by onboard electronics [7]. To this end, a simple inductive coupling to the power line might be employed. However, maintaining a constant power source is important for the system to be of practical use. If a power line experiences a fault or otherwise becomes inoperable, the sensor and transmitter must retain power in order to communicate the line's status. In a line power harvesting scheme, a "dead" line results in an inoperable transmitter and the sensor cannot communicate the necessary information.

To supplement harvesting power directly from the line, a battery might be placed on the transmitter to provide it with a constant power source in such a situation. In order improve the battery lifespan, the battery could be charged through the aforementioned power line energy harvesting method. This provides for a resilient transmitter which maintains operation during short power outages in the line being

measured. If the line is dead for an extended period of time, though, the battery might completely discharge and the transmitter will fail to operate. Over the lifetime of the sensor, the battery energy capacity might deteriorate and it may require replacement. Replacing components on high-voltage lines is a difficult and possibly expensive process. In a power grid with a massive deployment of sensors, this does not provide a viable solution in the long term [4].

Another option for powering the transmitter is energy harvesting from sources other than the power line itself. Solar and thermal energy harvesting do not provide a reliable source of power due to varying environmental conditions. RF energy harvesting, on the other hand, can be designed to provide a constant source of power and easy hardware accessibility for maintenance. With RF energy harvesting, the power source is decoupled from the high-voltage power line and can be easily repaired, replaced or modified. RF energy harvesting can also build upon the RF hardware used in the wireless communication link to minimize production cost.

RF energy harvesting involves a source and collector. The source emits an RF carrier wave at some known frequency, and the collector uses an antenna and charge pump to rectify the received RF energy to a DC voltage for easy consumption by other electronics. Passive Radio-Frequency Identification (RFID) provides an ideal platform for a robust high-voltage sensing system.

1.2 RFID

Radio-Frequency Identification (RFID) is a popular system for the wireless exchange of information commonly used in tracking, logistics, and identification. Common terminology in RFID defines the data receiver/power source as the *reader* and the data transmitter as the *tag*. There are three distinct categories of RFID: active, semi-passive, and passive. In active RFID, the tag provides its own source of power for the electronics and transmitter, such as through a battery. In semi-passive RFID,

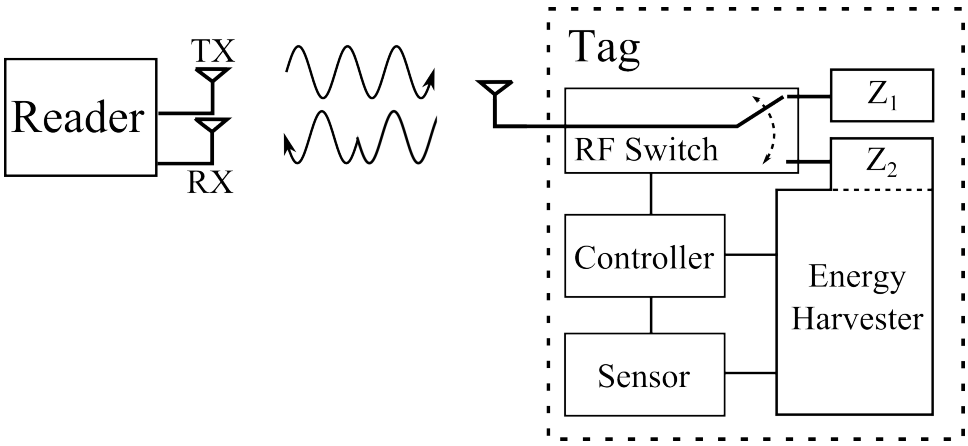

Figure 3: Basic diagram of a wireless current transformer sensor. The red is the power line and sensor at high potential and green is the receiver at ground potential. The sensor must now include circuitry for packetizing sensed current data and transmitting to the receiver.

the RFID provides its own source of power for the electronics. Neither semi-passive nor passive RFID provide their own RF carrier for transmitting data. Instead, they modulate data directly onto the carrier supplied by the reader and *backscatter* the modulated signal to the reader. Passive RFID, the RFID category referred to in this work, uses the reader's carrier for both backscattering data and powering the electronics through RF energy harvesting.

A backscatter wireless link is achieved through load modulation on the tag. A more detailed diagram of this system is shown in Figure 3. The reader transmits a continuous wave (CW) at some predefined frequency. The CW is received by the antenna on the tag and passed through an RF switch connected to two or more different loads. The loads are chosen based on the desired modulation technique. For example, an open and short load can be used for BPSK [8]. The different loads provide a different reflection coefficient for the received CW. Easily implemented loads used for modulation in semi-passive RFID tags are open and short, providing reflection coefficients of 1 and -1 respectively. The CW is modulated with the tag's data by switching between the two loads. For passive RFID tags, one of the loads is

chosen to be a charge pump which absorbs the incident power to harvest the energy, and thus ideally has a reflection coefficient of 0. This comes with the trade-off of having less signal power backscattered to the reader. The CW is reflected from the connected load back through the switch to the tag's antenna with an amplitude and phase defined by the reflection coefficient. This reflected waveform is radiated by the tag's antenna to the reader.

As with the physically wired sensor systems described earlier, passive RFID does have its trade-offs. The first issue is designing a tag which can be passively powered. This involves the design of a high gain antenna (provided the reader's position is known), efficient charge pump, and low power electronics. In addition, the wireless channel between the tag and reader should be well understood and accounted for in the communication *link budget*. A link budget is a simplified equation which relates the received signal power to transmitted power by quantifying the entire propagation chain in discrete gains and losses [8]. In a high-voltage sensing application, the link budget will additionally need to include effects in this unique environment, most notably, corona formation.

A corona is a plasma that forms at the surface of a conductor due to dielectric breakdown. In the case of high-voltage power lines, a large potential gradient exists at sharp points or corners of the conductor. If this is greater than the dielectric strength of the surrounding material (in this case air) then a corona may form. This is not the same as an arc in that an arc creates a stream of plasma between the high and low potential conductors, while the corona is simply a plasma layer surrounding one conductor. With an RFID tag on a high-voltage line, a corona may form at the antenna surface or edges. This conductive plasma layer can result in degraded communication performance. Understanding this phenomenon is vital to creating a reliable communication system for high-voltage sensing.

CHAPTER II

CORONA PLASMA

A plasma is a state of matter wherein a material contains a significant proportion of free ions and free electrons relative to neutral molecules. The specific ratio of ionized to non-ionized molecules in a plasma depends in part on the particular type and method of formation. If the free electron density of a plasma is high enough, it can act as a conductor, attenuating an electromagnetic wave, as well as detuning an antenna near it. Compared to free electrons, the ions in a plasma interact with an electromagnetic wave to a much lesser degree due to their much larger inertia. An antenna on a high-voltage power line may be subject to plasma effects due to the strong electric fields around it. The method of plasma formation around the antenna is called an *electrical breakdown*.

To be specific, the type of electrical breakdown to be discussed is the corona. A corona is an electrical breakdown of a gas at "high" pressure around a sharp electrode at high voltage. When discussing electrical breakdown of gases, high pressures include atmospheric pressure, which is 760 mm Hg, and low pressures are on the order of 1 mm Hg [1, p.476]. At low pressures, plasma formation is characterized by different breakdown mechanisms due to the decreased interactions between gas particles. At atmospheric pressure, the gas molecules have a high collision rate, affecting the breakdown significantly. Corona is the primary electric breakdown mechanism for high-voltage transmission lines in air at atmospheric pressure.

In addition to pressure, the composition of the gas and geometry of the electrodes greatly affect corona formation. As a result, simply knowing the electric field distribution in a volume is insufficient for predicting corona plasma formation. Gas

composition, which can vary greatly in air with humidity and particulate pollution, will affect plasma formation. The geometry of the electrodes, their material composition, microscopic surface deformities, foreign matter deposition on the surfaces, and presence of external ionizing sources like cosmic rays all play a large role in corona formation. As a result, the behavior of an antenna in a corona plasma is not absolutely predictable in all circumstances. Corona formation on an antenna deployed in the field will vary with mounting position, time of day, weather, and over the course of its lifespan. Modeling of these problems poses its own difficulties due to the significant impact of atomic scale phenomena on the macroscopic behavior. However, approximations and generalizations can be made in order to understand and mitigate issues arising from corona formation on an antenna.

In order to appreciate the problem of antenna performance in a corona, first the behavior and composition of the plasma must be understood. In simple terms, it can be stated that a corona plasma in air results from the presence of a strong electric field which provides the energy for plasma formation. The electric field is the result of an electric potential difference between two or more objects. The field with no plasma present can be found by solving Gauss's Law in the volume of interest (1).

$$\nabla \cdot \mathbf{E} = \frac{\rho}{\varepsilon} \tag{1}$$

In (1), $\nabla\cdot$ is the divergence operator, $\mathbf{E}$ is the electric field vector, ρ is the space charge density, and ε is the electric permittivity of the medium.

A simple yet illustrative geometry to consider in solving for the electric field around a high-voltage power line is an infinitely long cylinder above an infinite ground plane, as illustrated in Fig. 4. The cylinder here represents the geometry of a conducting power line. It can be observed that due to linearity, the electric field vector distribution is related to the potential difference between the power line and ground by a scalar value, provided the scenario can be approximated as being electrostatic. A

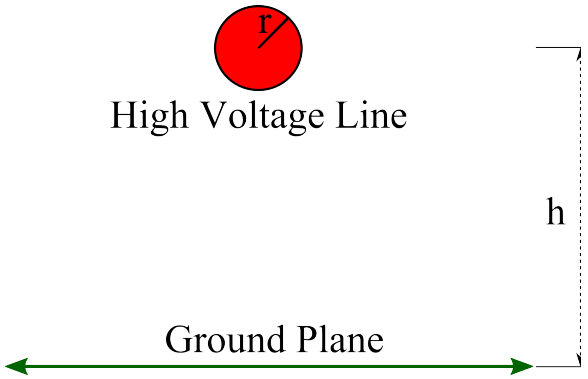

Figure 4: Cross section of a simple power line geometry. The red circle is the cross section of an infinitely long cylindrical conductor at some electric potential, and the green line represents an infinite ground plane.

negative scaling factor indicates a reversal in the direction of the electric field vector.

Using the software package COMSOL Multiphysics, Gauss's Law is solved for the geometry in Fig. 4 with dimensions of $r = 1cm$ and $h = 5m$. Since the cylinder is assumed to be infinitely long, the problem can be solved in the two-dimensional cross section solution space. The fields of interest in this problem surround the cylinder. In order to make the solution space finite while closely approximating infinite boundaries, the bounding box for the problem is chosen to be much larger than the radius of the cylinder. With a cylinder of radius $1cm$, the bounding box is chosen to be $12m$ wide and $10m$ tall, centered around the cylinder. The bottom boundary of the bounding box is set to ground potential, while the three other sides are set to a zero charge boundary condition, which essentially sets the normal electric field to zero, since the field on the outside of the boundary must be zero. (2). The cylinder is set to a potential of $1V$.

$$\mathbf{E} \cdot \hat{n} = 0 \tag{2}$$

The electric potential gradient, as well as the electric field lines can be seen in Fig. 5. The electric field magnitude as a function of distance from the surface of the

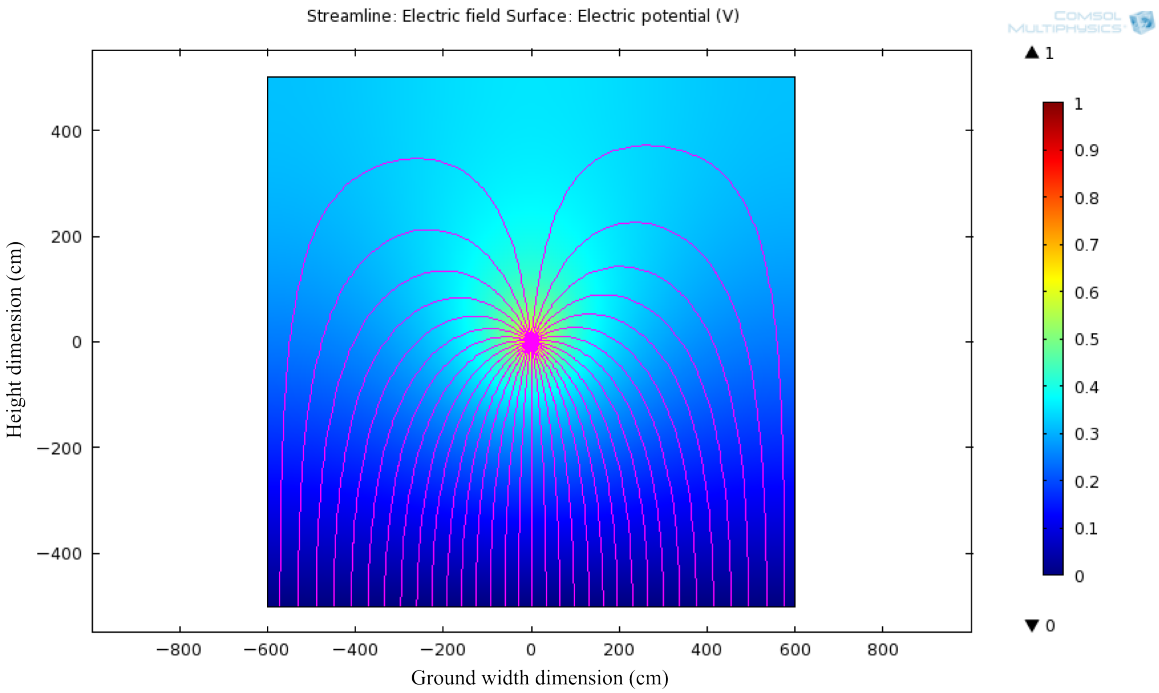

Figure 5: Voltage gradient and electric field lines computed for an infinitely long cylindrical conductor at $1V$ above an infinite ground plane. The cylinder has a radius of $1cm$ and is $5m$ above ground.

cylinder is plotted in Fig. 6. The field is measured downward, in the direction of the ground plane. The difference between the electric field above and below the cylinder is small ($< 2\%$), and the problem near the conducting cylinder could be approximated by a concentric cylinder geometry which is radially symmetric.

The result of interest in this example is the large electric field magnitude directly surrounding the wire. In a high-voltage power line application, small geometries such as sharp corners and thin wires produce around them extremely large voltage gradients. The electric field directly surrounding a point could be large enough to generate a corona. In creating a sensor for use on high-voltage power lines, it is important to avoid corners and points. Power engineers employ other corona mitigation techniques such as corona rings and specially braided power lines, which hinge on reducing the electric field magnitude around the lines [9].

High-voltage power transmission is predominantly done using *alternating current*,

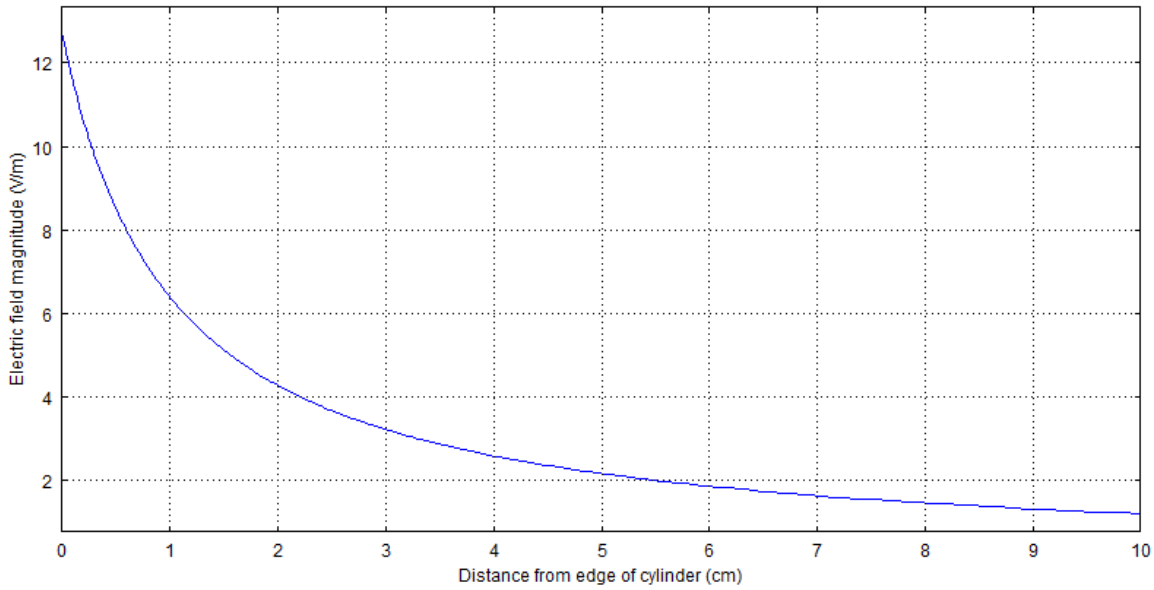

Figure 6: Voltage gradient and electric field lines computed for an infinitely long cylindrical conductor at $1V$ above an infinite ground plane. The cylinder has a radius of $1cm$ and is $5m$ above ground.

or AC, because of the ease of transforming voltages and currents. This means that the voltage of the power line examined in Figs. 4-6 varies sinusoidally, at a frequency of $50 - 60Hz$ in the United States, and can be either positive or negative relative to ground. The strong electric field around the power line will either be pointing away from or toward the line. This leads to two more factors that affect corona formation, the polarity of the conductor producing the corona, and the frequency of the alternating voltage. Following is a discussion of the negative and positive corona phenomena.

2.1 Negative Corona

A negative corona is a corona that forms around the cathode, or negative voltage terminal. In the geometry of Fig. 4, a negative corona would form around the high-voltage line if the line is at a negative electric potential relative to the ground plane. It is not self-sustaining, meaning its electron and ion distribution will cause itself to

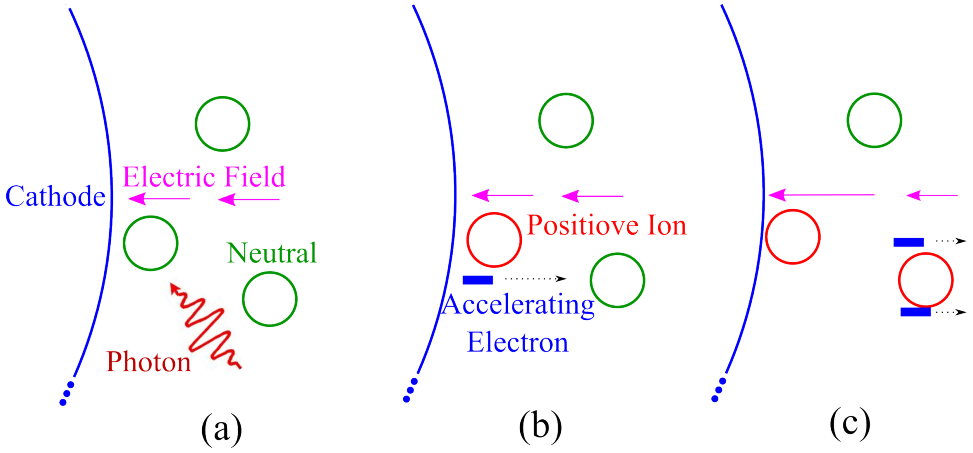

Figure 7: A diagram of the process of negative corona formation. (a) An energetic photon collides with a neutral molecule at the surface of the cathode. (b) The molecule is ionized into a positive ion and electron. The electron with a low mass is accelerated away from the cathode by the strong electric field. (c) The energetic electron collides with a neutral molecule ionizing it. The resulting electrons accelerate away from the cathode more slowly because of the weaker electric field at this distance. The massive positive ions slowly accelerate toward the cathode.

extinguish only to be regenerated, leading to a high frequency ionization/quenching cycle (relative the the $60Hz$ line frequency). The process for negative corona formation is as follows.

2.1.1 External ionization of molecules

In order for a corona plasma to begin formation, there must be an external ionization source to excite and ionize a small number of molecules. This is a continuously occurring process in the atmosphere, where molecules are constantly being ionized by sources such as cosmic rays and then recombining. Fig. 7 illustrates this process. In Fig. 7(a), the surface of the cathode is shown with neutral gaseous molecules surrounding it. The electric field represented by the solid magenta vectors is pointing into the cathode. This is a molecular level model of the macroscopic geometry illustrated in Figs. 5-6. The photon in Fig. 7(a) ionizes a neutral molecule into a positive ion and electron, shown in Fig. 7(b).

2.1.2 Electron avalanche

The free electrons near the surface of the cathode are accelerated by the strong electric field away from the cathode. The positive ions are accelerated toward the cathode. However, the ions are several orders of magnitude more massive than the electrons, and therefore their distance traveled over the same period of time is several orders of magnitude lower than that for electrons in an equal electric field. For example, a single ion of Nitrogen gas (N_2, the most abundant molecule in air) is approximately $51,000$ times more massive than an electron.

Accelerated by the electric field, the electron may gain enough kinetic energy to ionize a second molecule as illustrated by Fig. 7(c). The energy necessary for ionization depends on the molecule being ionized, such as oxygen or nitrogen. The two electrons are then accelerated away from the cathode, and may continue in an avalanche of ionizations. The excitation of molecules also releases photons, leading to a visible glow from the ionization region. At a certain distance from the cathode, the electric field magnitude will be too weak to accelerate the electrons to a kinetic energy capable of ionizing another molecule.

The weakening of the electric field away from the cathode is a function of geometry and charge accumulation. The geometrical dependence of the electric field is illustrated in Figs. 5,6. Charge accumulation is illustrated in Fig. 7(c). When electrons move away from the cathode, the slower moving positive ions are left behind. This creates a net positive space charge around the cathode. According to Gauss's Law (1), a space charge in a volume creates an electric field, which in turn affects the motion of the charges, etc. The positive ion buildup at the cathode "shields" the volume beyond it from the cathode's electric field, and there is a field enhancement between the positive ions and the cathode.

2.1.3 Extinguishing

The enhanced electric field in the small gap between the cathode and positive ions increases the force between them, accelerating the ions to the cathode. When the positive ions collide with the cathode, they bond with a free electron on the conductor and neutralize. The short region of high electric field diminishes. Some positive ions may also collide with the cathode with enough energy to ionize a molecule, creating another electron avalanche. The electrons from the avalanche continue toward the ground plane, or anode, slowing down considerably. Many low energy electrons at a distance from the cathode bond with gas molecules, such as oxygen (O_2), creating slower negative ions, which also travel toward the anode. Once the negative ions reach the anode, they neutralize as did the positive ions.

Throughout this process of ion drift and neutralization, the electric field distribution in the volume relaxes closer to its neutral state. Once enough positive ions at the cathode have been extinguished, the electric field becomes strong enough again to accelerate an electron to an ionizing energy, and the corona formation repeats. The frequency of corona formation and extinguishing, as with any electrical breakdown, depends on my factors including the cathode point size (geometry), potential, and gas composition. Generally speaking, the frequency will increase with higher potential, and also with a sharper point at the cathode. The frequency has been measured on the order of kiloHertz in air at atmospheric pressure [1, p.518].

2.2 Positive Corona

A positive corona is a corona that forms around the anode, or positive terminal. In the geometry of Fig. 4, a positive corona would form around the high-voltage line if the line is at a positive electric potential relative to the ground plane. It can be a self sustaining discharge. The process for positive corona formation is as follows.

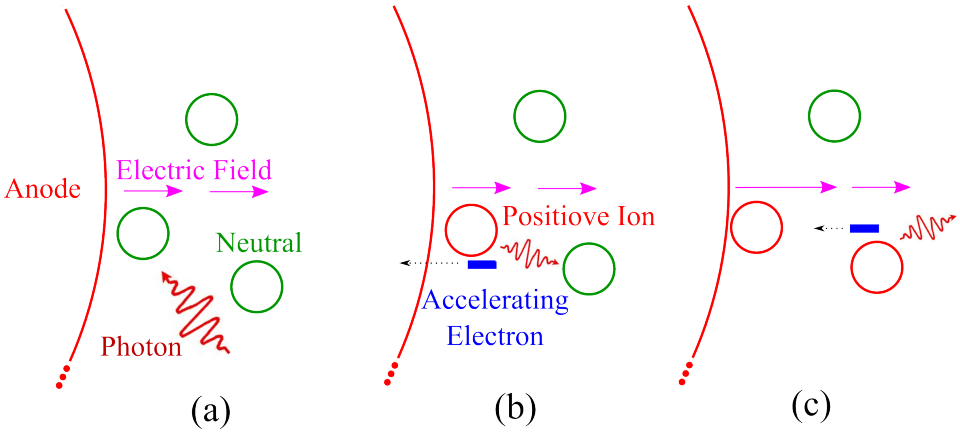

Figure 8: A diagram of the process of positive corona formation. (a) An energetic photon collides with a neutral molecule at the surface of the anode. (b) The molecule is ionized into a positive ion and electron, or excited to release a photon. The electron with a low mass is toward the anode by the strong electric field, exciting and ionizing subsequent molecules. (c) The free electrons are abosrbed by the anode upon collision. Through photoionization and field enhancement due to the positive ions, electrons are produced farther away from the anode, creating a self-sustaining positive corona once an equilibrium of ionization and recombination is achieved.

2.2.1 External ionization of molecules

Like the negative corona, a positive corona is initiated by the ionization of molecules near the anode by an external source, such as a high energy photon, as shown in Fig. 8(a). The free electron generated in the ionization of a neutral gas molecule near the anode will be accelerated toward the anode. Unlike in the case of the negative corona, as the electron moves toward the anode, the electric field becomes stronger, not weaker. The massive positive ions slowly move away from the anode.

2.2.2 Secondary photoionization

The freed electrons excite or ionize other molecules very close to the anode as they accelerate toward it. The newly generated electrons continue in a short avalanche of subsequent ionizations toward the anode. The electrons are absorbed at the anode, leaving behind a volume of positive ions near the anode surface, Fig. 8(b).

The molecules excited by the electrons near the anode emit energetic photons

when their electrons fall back into the ground state. The photons in turn ionize more molecules farther away from the anode, in a process called *photoionization*. Due to the newly created positive space charge around the anode, the electric field is intensified farther away from the anode surface. Electrons generated by photoionization farther away from the anode surface can now be accelerated to an energy by which they ionize more molecules as they travel toward the anode. This secondary avalanche of electrons excites and ionizes molecules similar to the first wave, Fig. 8(c) [10, p.308].

2.2.3 Self-maintaining corona

Photoionization of molecules farther away from the anode continues until a steady state is reached where the electric field from the anode, positive ion volume charge density, and electron volume charge density is just strong enough at a certain distance to ionize subsequent molecules. As positive ions drift out toward the cathode, more positive ions are generated at the anode, and neutral molecules are generated through recombination and travel through diffusion.

2.3 AC Corona

High-voltage power transmission lines predominantly use alternating current (AC) due to the ease of transforming voltages and currents. The positive and negative corona discussed above reference the DC voltage breakdown cases. On a high-voltage AC line, the positive and negative corona will alternate at the frequency of the voltage, $60Hz$ in the United States. The question arises of how the oscillation of the voltage might affect the corona formation.

The corona formation phenomena such as ionization and electron drift described above happen on the order of $1\mu s$ [1, p.550]. This is much faster than the oscillation of line voltage. Therefore, a simplifying assumption can be made that at any particular instance, the corona on the line is equivalent to the corona that would form if the line were at that DC voltage. However, the ion mobility can still play a factor in corona

formation.

Taking the negative corona as an example, the negative ions formed farther away from the cathode slowly drift toward the anode, or ground. As the line potential swings from negative to positive, any negative ions in the space that have not reached the ground and been neutralized will remain in the space and begin accelerating toward the line, now the cathode. The negative ions in the space between the positive line and ground increase the electric field intensity at the line according to Gauss's Law (1). The electric field enhancement at the line decreases the potential needed for corona onset. Therefore, the corona onset voltage can actually decrease when using AC voltages, as compared with the DC corona. In addition, corona can exhibit a hysteresis where the electric potential needed to maintain a corona is lower than the startup potential. The corona can persist for a short time after the line voltage has fallen below the voltage at which the corona was initiated [11],[12],[13].

2.4 Methods for corona prediction

Many studies have been carried out in plasma physics, and many theories developed regarding corona formation. Studies in electrical discharges, including corona, have predominantly been performed on small scales in very specific geometries and gasses. Commonly used electrode pair geometries include coaxial, parallel cylindrical lines, adjacent spheres, and point-to-plane [10, p.302],[14, p.148]. The studied geometry sizes typically fall on the order of centimeters for practical reasons. Smaller geometries are easier and less costly to manufacture, and require lower voltages for corona onset. Many of these studies are cited in Loeb [1], Maxfield [10], and Meek [14], who have written books on the subject of electrical discharges in gasses.

Methods for corona prediction and simulation exist which can aid in high-voltage equipment design. Empirical measurements led Townsend to deduce the relationship

between the number of electrons produced through electron collision over a specified path and the ratio of electric field strength to gas pressure for various gases [15]. This relationship is characterized by Townsend's first ionization coefficient. Townsend's second ionization coefficient similarly relates the number of electrons generated through positive ion collision to the electric field and pressure over a path. Phillips [16], Abdel-Salam [17], and Pedrow [18] have performed analyses of corona formation using the Townsend models for ionization.

Using a kinetic Boltzmann model, electrical discharge plasma formation has also been simulated and studied by Rodriguez [19], Farouk [20], Cristina [21], and Chen [22],[23] among others. One useful result from empirical studies is the approximate *dielectric strength* of air and other dielectrics. The dielectric strength is the approximate uniform electric field magnitude required to initiate an electrical breakdown in a dielectric, corresponding to a field capable of creating an electron avalanche. This is useful for order of magnitude approximations when trying to determine the likelihood of corona formation. The dielectric strength of air at atmospheric pressure is approximately $30kV/cm$ [24].

2.4.1 Peek's law

One of the early contributors to corona theory was John S. Townsend. Townsend, after whom the ionization coefficients are named, uncovered the ionization mechanisms in gas discharges. From the knowledge of these mechanisms, one can predict corona behavior given empirically derived values of the Townsend coefficients. Another important contributor to the field was Frank W. Peek, Jr. Peek is well known for his empirical formulation of corona onset behavior for the case of two parallel wires, useful in high-voltage transmission line engineering.

Peek's law for parallel wires can be stated in two equations. The first equation gives the electric field magnitude at the surface of the wire, termed in his writings as

Table 1: Table of terms used in Peek's law for parallel wires (3),(4). ρ_{STP} is the air density at Standard Temperature and Pressure.

Variable	Description	Typical value in air	Units
E_v	Visual critical gradient	n/a	kV/cm
E_o	Disruptive critical gradient	30 (DC voltage), 21.2 (AC RMS voltage)	kV/cm
C	Empirical geometrical constant	0.301	$cm^{1/2}$
δ	Relative air density	ρ/ρ_{STP}	1
r	Wire radius	n/a	cm
V_v	Spark-over voltage	n/a	kV
m_v	Irregularity factor of conductor surface	1 (smooth), < 1 (rough)	1
S	Spacing between conductor centers	n/a	cm

the visual critical gradient, at which a visible corona will develop around the wire (3) [25].

$$E_v = E_o\delta\left(1 + \frac{C}{\sqrt{\delta r}}\right) \tag{3}$$

The second equation relates the critical visual gradient, E_v, to a corresponding spark-over voltage, V_v, based on the wire radius and separation (4) [25].

$$V_v = E_v m_v r \ln\left(\frac{S}{r}\right) \tag{4}$$

The terms from (3) and (4) are described in Table 2.4.1. ρ_{STP} is the air density at Standard Temperature and Pressure. The disruptive critical gradient, E_o, is different for the DC and AC ($60Hz$) voltage cases. For wires with a DC voltage, the value of E_o is $30kV/cm$, as given at the end of the previous section. Given an AC RMS voltage, the critical gradient is $30/\sqrt{2} = 21.2kV/cm$ [25].

When dealing with a high-voltage power line above a ground plane as in Fig. 4, Peek's law can be adjusted using the method of images. If there exists a voltage V_v between two parallel wires, the geometry can be interpreted as in Fig. 9, where one wire is at a voltage of $+V_v/2$ and the other is at a voltage of $-V_v/2$. Using the method of images, the geometry can be interpreted as a wire above a ground plane, where the height of the wire is $h = S/2$, and the voltage of the wire with respect to

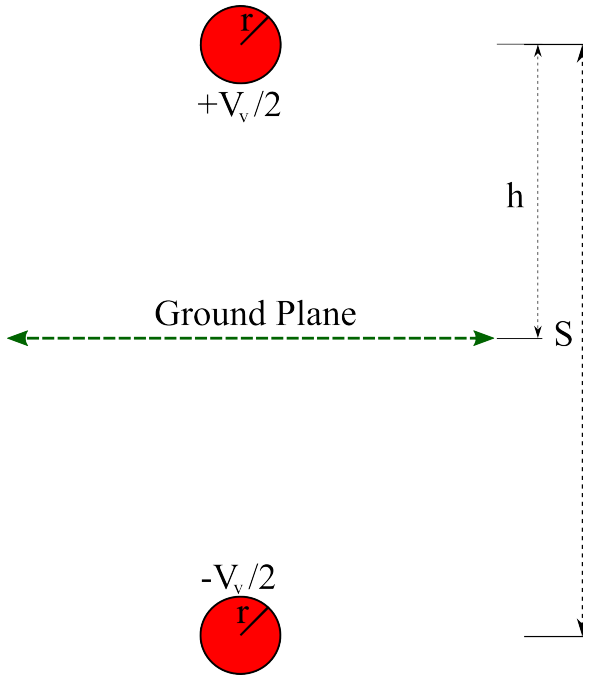

Figure 9: Cross section of a simple power line geometry with its relation to a parallel wire geometry. The red circles are the cross sections of two infinitely long cylindrical conductors at opposite electric potentials, and the green line represents an infinite ground plane.

the ground plane is $V_v/2$. The second equation of Peek's law (4) can then be restated as (5), where V_{vg} is now the voltage of the wire with respect to the ground plane, and h is the height of the wire above the ground plane.

$$V_{vg} = \frac{1}{2} E_v m_v r \ln\left(\frac{2h}{r}\right) \tag{5}$$

As an example of how Peek's law might be used, let us assume there is a smooth high-voltage AC power line $5m$ above the ground with a radius of $1cm$. The air is at Standard Temperature and Pressure. The RMS voltage at which visible corona formation could appear would be:

$$V_{vg} = \frac{1}{2} E_v m_v r \ln\left(\frac{2h}{r}\right)$$
$$V_{vg} = \frac{1}{2}\left[E_o \delta\left(1 + \frac{C}{\sqrt{\delta r}}\right)\right] m_v r \ln\left(\frac{2h}{r}\right)$$

$$= \frac{1}{2} \times 21.2 \times \frac{\rho_{STP}}{\rho_{STP}} \times \left(1 + \frac{0.301}{\sqrt{1 \times 1}}\right) \times 1 \times 1 \times \ln\left(\frac{2 \times 500}{1}\right)$$
$$= 95.3kV$$

Using Peek's law, simple estimates can be made for the feasibility of corona formation on high-voltage power lines. However, one must always remember that addition of complex conductor geometries can drastically change corona behavior. Studies of complex corona formation criteria and scenarios are beyond the scope of this work. However, armed with the basic theory of corona formation, we now apply the physical behavior to antenna radiation behavior.

CHAPTER III

ELECTROMAGNETIC WAVE PROPAGATION IN AN ISOTROPIC CORONA PLASMA

Electromagnetic waves consist of oscillating transverse electric and magnetic fields. When an electromagnetic wave propagates through a plasma, it is attenuated due to the energy imparted to the free electrons in the plasma and lost through their collisions with other molecules. As stated earlier, the effect of ions on an electromagnetic wave in a plasma can be neglected because of their large inertia compared to electrons, and thus the small amount of energy they gain from the wave. Therefore, the behavior of an electromagnetic wave propagating through a plasma can be determined by the interaction of the wave with a volume of free electrons. The solution to (6) gives the effective material parameters of a plasma which can be used in further electromagnetic modeling, such as that of antennas. The plasma can essentially be treated using the Drude model for electrical conduction. Here, the direction of the force is chosen to be in the x-direction without loss of generality.

$$F = m_e\ddot{x} = -eE - \nu m_e\dot{x} \tag{6}$$

In (6), m_e is the electron mass (kg), x is the electron displacement (m), e is the electron charge (C), E is the electric field intensity (V/m), ν is the electron collision frequency (Hz), $\dot{x}$ is the first time derivative of x (m/s), and $\ddot{x}$ is the second time derivative of x (m/s^2). The electron collision frequency increases with the density of the gas, and provides damping to the oscillation of the charges through collisions. For air at atmospheric pressure, the collision frequency is on the order of $1THz$ [26]. From (6), the relative complex permittivity of the plasma can be determined as a

function of the plasma electron density and wave frequency (7). The term ω_p is called the plasma frequency, and is the natural frequency of oscillation of the free electrons (8).

$$\varepsilon_r = \varepsilon_\infty - \frac{\omega_p^2}{\omega(\omega - j\nu)} \tag{7}$$

$$\omega_p = \sqrt{\frac{n_e e^2}{m_e \varepsilon_o}} \tag{8}$$

The value ε_r is the relative permittivity of the plasma, ε_∞ is the relative permittivity of the un-ionized gas (1 for air), ω_p is the plasma frequency (rad/s), ω is the electromagnetic wave frequency (rad/s), n_e is the electron density (m^{-3}), ε_o is the permittivity of free space (F/m) [27].

For a low pressure plasma, the collision frequency is small and can be neglected in (7) when considering a high frequency electromagnetic wave ($\nu << \omega$). There exist two modes of propagation due to the dispersive nature of the plasma:

1. $\omega < \omega_p$:

   γ, the propagation constant, is completely real so there is no propagation through the plasma. The wave is reflected from the surface.

2. $\omega > \omega_p$:

   γ, the propagation constant, is completely imaginary so the wave passes through the plasma unattenuated.

The plasma frequency increases proportionally to the square-root of the electron density, as seen in (8). In order to communicate through a channel containing a low pressure plasma, a high carrier frequency would be used, such that the wave frequency is greater than the plasma frequency (i.e. $f > \omega_p/2\pi$). A typical arc discharge, which would constitute the complete breakdown of the air between the high-voltage

electrode (wire) and ground, has a typical electron number density on the order of $n_e \sim 10^{21} m^{-3}$ [28]. A strong corona plasma could have an electron number density on this order or lower. Taking a practical number density for a corona plasma of $n_e \sim 10^{19} m^{-3}$, the plasma frequency would be on the order of $\omega_p \sim 10^{11} rad/s$. RF communication in the $f \sim 100GHz$ region would be one solution to the problem of propagation in a low pressure plasma. This result, while illustrative of the behavior of some plasmas, is applicable specifically to a low pressure plasma. In air, the number density of molecules ($\sim 10^{25} m^{-3}$) is large enough that the collision frequency (or damping term) in (7) is not negligible.

Due to the relatively high pressure involved in a corona plasma ($1atm$, as compared with $10^{-3} atm$ for a high-voltage glow discharge, or $10^{-5} atm$ in the ionosphere), energy loss due to electron collisions with molecules is not insignificant. At standard temperature and pressure, a Maxwell-Boltzmann speed distribution for electrons coupled with the density of air molecules results in an average collision rate of $\nu = 10^1 2 sec^{-1}$ [26]. Since the collision frequency is larger than practical communication frequencies, the collision term from (7) is not negligible. Practical communication frequencies are those that lie in ISM (Industrial, Scientific, and Medical) radio bands and allow for low cost RF hardware manufacture. Also, RF energy harvesting efficiency decreases with frequency due to the intrinsic junction capacitance of the diodes in a charge pump. The $915MHz$, $2.45GHz$, and $5.8GHz$ ISM bands are commonly used in low-cost RFID systems.

From the complex dielectric constant (7), one can deduce the propagation constant as with the low-pressure case. The propagation constant can be written as (9), where ε_r is taken from (7). Here, α is the attenuation constant (Np/m), and β is the phase constant (rad/m).

$$\gamma = \alpha + j\beta = j\sqrt{\varepsilon_r}\frac{\omega}{c} \tag{9}$$

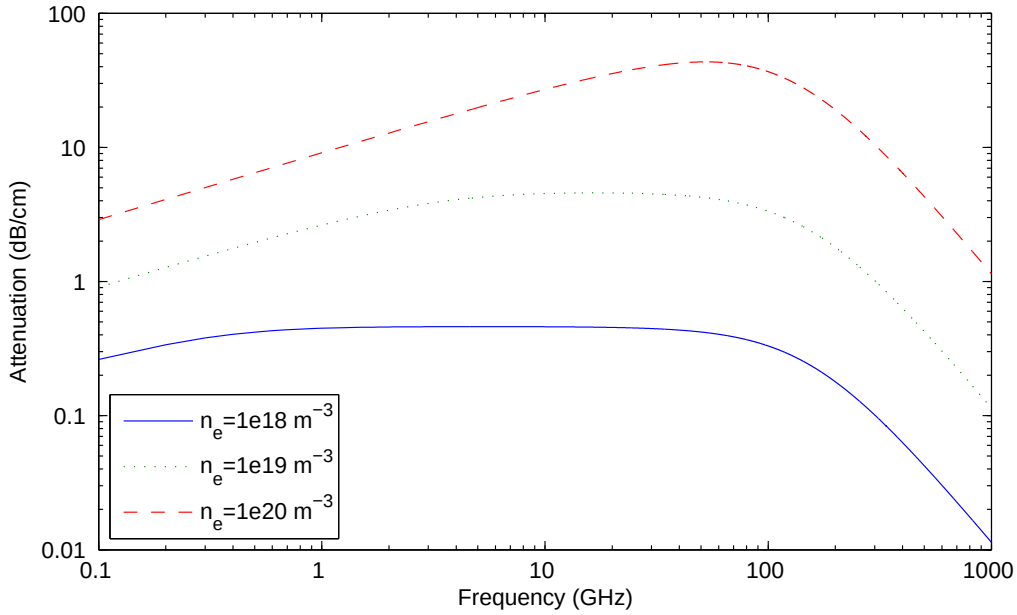

Figure 10: Attenuation of an electromagnetic wave through a plasma volume density vs. wave frequency. A Drude model is used with $\varepsilon_\infty = 1$ and $\nu = 10^{12} Hz$. The electron number density, n_e, dependence is shown for three typical values for a corona plasma.

The attenuation constant is plotted vs. electromagnetic wave frequency ($f = \omega/(2\pi)$) in Fig. 10 for various plasma electron densities. Fig. 10 uses an electron collision frequency of $\nu = 10^{12} Hz$. Fig. 11 is the same plot with a collision frequency of $\nu = 10^{2} Hz$ to illustrate the attenuating behavior of a low pressure plasma. In the low pressure case, the attenuation drops off sharply around at the plasma frequency. Below the plasma frequency, the value of the attenuation constant is not large when compared with 10. However, the propagation constant below the plasma frequency is purely real (0 phase constant), indicating an evanescent wave. A detailed derivation and analysis of the Drude model can be found in [27].

In the case of an atmospheric pressure plasma, the plasma is conducive to propagating modes at all frequencies. However, the attenuation varies with wave frequency,

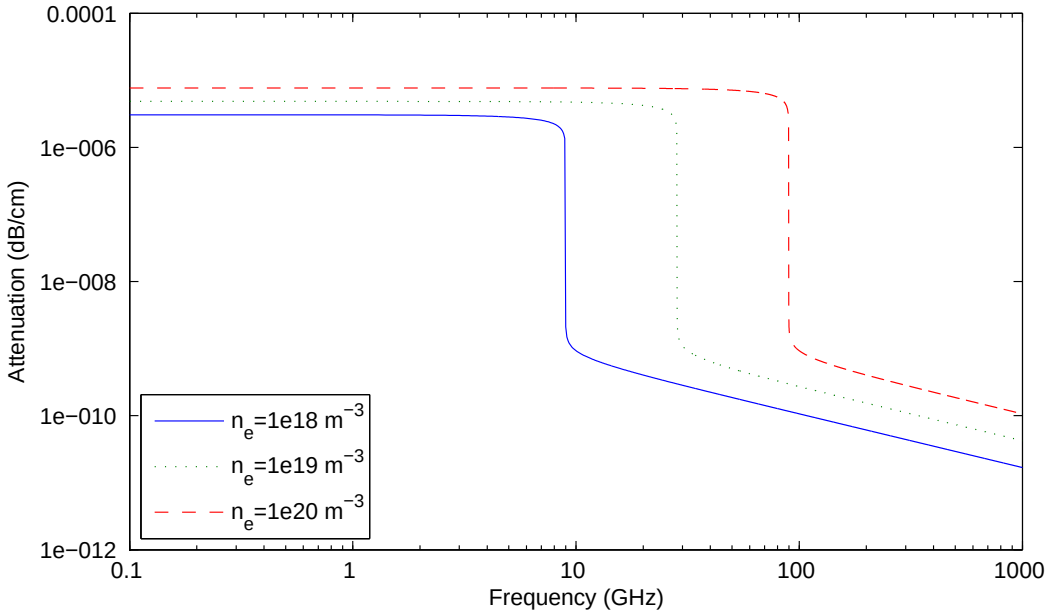

Figure 11: Attenuation of an electromagnetic wave through a plasma volume density vs. wave frequency. A Drude model is used with $\varepsilon_\infty = 1$ and $\nu = 10^2 Hz$. The electron number density, n_e, dependence is shown for three typical values for a corona plasma.

electron density, and collision frequency. A constant collision frequency can be assumed throughout the plasma since the neutral molecule density in air ($\sim 10^{25} m^{-3}$) is much greater than the ion and electron densities ($< 10^{21} m^{-3}$), so the electron collisions with the neutral molecules dominate this term.

From Fig. 10 and a mathematical analysis of the Drude model for electromagnetic wave propagation ([27],[26]), a few useful observations can be made:

1. The attenuation (α) increases with frequency until a break frequency of $f_{b1} = {\omega_p}^2/(2\pi\nu) Hz$ where it flattens out. Since ω_p increases with electron density, f_{b1} is seen to increase with electron density as well. A visual analysis of the slope indicates that $\alpha \propto \sqrt{f}$ below f_{b1} for the case of $\nu = 10^{12} Hz$. Studies of plots with much smaller and larger values of ν show that this observational approximation does not hold when ν is more than a few orders of magnitude grater than or less than ω_p. However, for atmospheric pressure corona, this

approximation is valid. In the case of a low pressure plasma where $\nu \ll \omega_p$, this first break frequency $f_{b1} \rightarrow \infty \gg f_{b2}$, resulting in a constant attenuation with frequency until it falls off at f_{b2}.

2. The attenuation decreases with frequency below a break frequency of $f_{b2} = \sqrt{|\nu^2 - w_p^2|}/(2\pi)Hz$. Since $\nu >> \omega_p$ in all three cases, this second break frequency is dominated by the collision frequency, and thus is the same for all three electron densities. A visual analysis of the slope indicates that $\alpha \propto 1/f^2$ above f_{b2} for the case of $\nu = 10^{12}Hz$. Again, this relationship breaks down and much higher and lower collision frequencies but is valid in the range useful for atmospheric pressure corona plasma studies. In the case of a low pressure plasma where $\nu << \omega_p$, the second break frequency is dominated by the plasma frequency, and thus a lower plasma density will have a lower break frequency f_{b2}.

3. Attenuation increases with electron density. When the collision frequency is large compared to the plasma frequency, as in Fig. 10, the attenuation increases linearly with electron density in the peak attenuation region.

Given these observations, several conclusion can be made:

1. A typical corona plasma is on the order of millimeters in thickness [1, p.520], and the peak electron density region of the corona comprises an even smaller fraction of this thickness. A plasma whose electron density is less than $n_e = 10^{18}m^{-3}$ does not pose a threat to an RF communication link due to attenuation alone, assuming the energy loss from an antenna covered in a plasma medium is on the order of a plane wave passing through the same plasma medium.

2. The frequency of operation to choose for an RF communication system should be chosen to be low. Because f_{b2}, as described in the above observations, is

dominated by the electron collision frequency, attempting to operate above this region may be impractical or cost prohibitive ($f > 100GHz$). One notices that, since only plasmas with electron densities greater than $n_e = 10^{19}m^{-3}$ will affect the communication link to a significant extent, the ISM bands ($915MHz$ - $5.8GHz$) lie largely below f_{b1}. Attenuation in this region is proportional to $\sqrt{f}$. Therefore, choosing a low frequency will decrease the attenuation of the wave by the plasma. This conclusion does not regard the communication path loss which is also a function of frequency.

As an illustration of the attenuation of an electromagnetic wave by an atmospheric pressure plasma, the $915MHz$ and $5.8GHz$ ISM frequencies can be compared. Taking the attenuation to be in region below f_{b1} where $\alpha \propto \sqrt{f}$, the ratio of attenuations of these two waves will be

$$\frac{\alpha_{5.8GHz}}{\alpha_{915MHz}} = \frac{\sqrt{5800}}{\sqrt{915}} = 2.52$$

This ratio is in terms of dB/cm. Therefore, an attenuation of $1dB/cm$ at $915MHz$ corresponds to $2.52dB/cm$ at $5.8GHz$. Likewise, an attenuation of $10dB/cm$ at $915MHz$ corresponds to $25.2dB/cm$ at $5.8GHz$. It is obvious that significant losses can be incurred due to a corona plasma at higher frequencies.

This section has looked at the attenuation effects of an isotropic atmospheric pressure plasma on an electromagnetic wave at various frequencies. This is one aspect of the corona on antenna problem. Besides attenuating an incoming or transmitting signal, the corona may affect the radiating characteristics of an antenna. Because a corona plasma is essentially a volume of free ions and electrons, it acts as a poor conductor. With a conducting corona surrounding an antenna, its resonant characteristics can be affected, further deteriorating communication performance. In order to understand how an antenna would operate with a corona buildup on its surface, simulations can be performed to obtain both the power loss and antenna resonance changes.

CHAPTER IV

RECTANGULAR PATCH ANTENNA PERFORMANCE IN A CORONA PLASMA

4.1 Antenna Basics

In order to radiate efficiently, an antenna is designed to resonate at the desired communication frequency. The *resonant frequency* of an antenna is a function of its geometry. At the resonant frequency, the input terminal impedance of the antenna is purely real, meaning that the antenna is purely resistive. *Impedance* is the complex ratio of voltage to current, such that a complex part would indicate reactive energy storage in the antenna. A change in the geometry of the antenna or its surroundings, including a corona plasma, can *detune* the antenna, meaning shift its resonant frequency or increase its reactance, reducing radiation at the intended frequency of operation [29]. The *return loss* is the ratio of the power available to an antenna to the power accepted by the antenna, and is a function of the antenna input impedance and source impedance it is connected to. The real part of the antenna input impedance at the frequency of operation is the *radiation resistance* of the antenna, and the current squared multiplied by the radiation resistance gives the power dissipated by the antenna. This is true for a lossless antenna, meaning its conductors have infinite conductivity and dielectrics have zero conductivity. All the dissipated power represents radiated power. In practical antenna design, this is impossible, as conductors like copper and dielectrics like FR4 are not ideal. The *radiation efficiency*, η_{rad}, of an antenna represents the ratio of the power radiated by the antenna to the power accepted by the antenna (10).

$$\eta_r ad = \frac{P_{rad}}{P_{acc}} \tag{10}$$

In (10), η_{rad} is the radiation efficiency, P_{rad} is the antenna radiated power (W), and P_{acc} is the power accepted by the antenna (W) from its power source, or generator. An antenna with a radiation efficiency of 1 is lossless, with values between 0 and 1 covering the domain of efficiencies for lossy antennas. Combined with the return loss, we can get the *total efficiency*, η_{tot}, of the antenna, which is the ratio of the power radiated by an antenna to the power available from the generator. Due to reciprocity, if the efficiency of the antenna is solved in the transmit mode, the same result can be applied to the receiving mode provided the medium is linear [30]. This is true for the other antenna properties discussed as well.

The *radiation pattern* of an antenna illustrates the proportion of power that is radiated in any given direction from the antenna normalized to the total radiated power. The *directivity* (D) is the maximum value of the radiation pattern. Thus, directivity indicates how much of the antenna's power is radiated in its main direction of transmission. The *gain* (G) of an antenna is the directivity scaled by the radiation efficiency (11). An antenna radiation pattern can can have its peak value scaled to either the directivity or gain, and is referred to as a directivity or gain pattern respectively.

$$G = \eta_{rad} D \tag{11}$$

The reader can refer to Balanis [30] for further reading on antenna fundamentals and design.

4.2 Rectangular patch antenna in corona simulation setup

In order to understand how an antenna behaves under the influence of corona plasma effects, finite-difference time-domain (FDTD) simulations are performed using CST Microwave Studio. The primary antenna to be simulated is the rectangular patch antenna. In order to perform a worst case evaluation of antenna performance in a plasma, the frequency of operation is chosen as $f = 5.8GHz$, as opposed to $2.4GHz$

or $915MHz$. According to the attenuation results in 10, plasma attenuation at higher frequencies ($915MHz$, $2.4GHz$) is expected to be higher (provided the frequency is below $100GHz$). A layer of plasma with a set thickness at the surface of an antenna is also expected to detune a higher frequency antenna by a greater amount. Detuning refers to the change in the antenna input impedance from the designed impedance in free space. At higher frequencies, the wavelength is shorter, so the constant plasma thickness corresponds to a larger fraction of a wavelength. The patch antenna is chosen due to its simplicity in design and manufacture, coupled with its relatively high directivity. The directivity of the $5.8GHz$ patch calculated in CST is $D = 7.16dBi$. Here, dBi is the unit which normalizes the antenna under test to a perfect isotropic radiator.

The rectangular patch is first designed to operate at a frequency of $5.8GHz$ [30]. An image of the patch from CST is shown in Fig. 12. The patch is fed from the bottom through a coaxial cable in order to avoid interaction of the plasma with the feed. In simulation, the plasma is placed over top the antenna on the side opposite the ground plane, so a microstrip feed in the plane of the antenna would couple into the plasma as well, possibly altering the results. For the patch, realistic lossy materials are used so the radiation efficiency is less than 1. A screenshot of the patch antenna used for simulation is shown in Fig. 12. Figs. 37,39,40,41 in Appendix A show a diagramatic view of the antenna from different angles with all relevant dimensions labeled. The FR4 substrate is not depicted in the figures for ease of viewing. As seen in Fig. 12, the substrate extends from the top of the ground plane to the bottom of the patch antenna, and extending to the edges of the ground plane. A table of dimensions for the patch antenna is given in Table A in Appendix A. The dielectric substrate used for the patch (shown in green in Fig. 12 is FR4 with a relative permittivity of $\varepsilon_{r,FR4} = 4.1$ and a dielectric loss tangent of $tan\delta_{FR4} = 0.016@1GHz$. The insulator for the coaxial feed line is PTFE with a relative premittivity of $\varepsilon_{r,PTFE} = 2.1$ and a

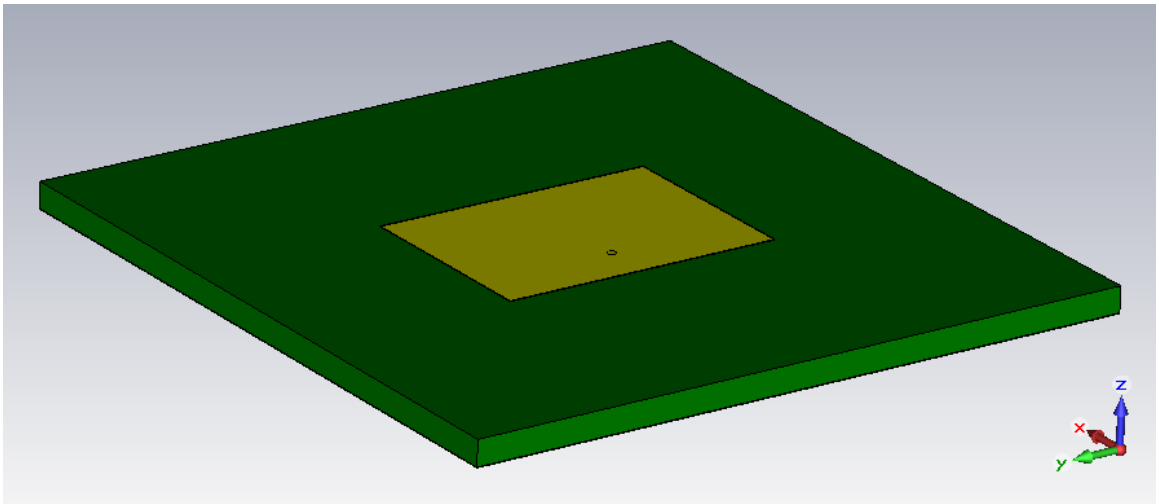

Figure 12: Screenshot of $5.8GHz$ rectangular patch antenna designed and simulated in CST Microwave Studio. The yellow material represents copper, and the green material represents FR4 dielectric.

Table 2: Simulated characteristics of the $5.8GHz$ rectangular patch antenna from CST Microwave Studio.

Parameter	Value	Units
Frequency	5.8	GHz
Directivity	7.16	dBi
Gain	5.87	dBi
Radiation Efficiency	74.4	%
$-10dB$ Bandwidth	4.7	%
Input Impedance	$49.37 - 0.54i$	Ω

loss tangent of $tan\delta_{PTFE} = 0$.

The directivity of the patch antenna is plotted in Figs. 13-14. The return loss of the antenna is plotted in Fig. 15 referenced to 50Ω. The characteristics of the patch antenna are given in Table 4.2.

With the basic rectangular patch antenna characterized, a plasma is applied to it in CST Microwave Studio for simulation and analysis. The plasma material is simulated in CST using its built-in Drude material model, as described in (7). CST takes as inputs the plasma frequency, which can be derived from (8) for a specific electron density, collision frequency, and ε_∞, the relative dielectric constant of the

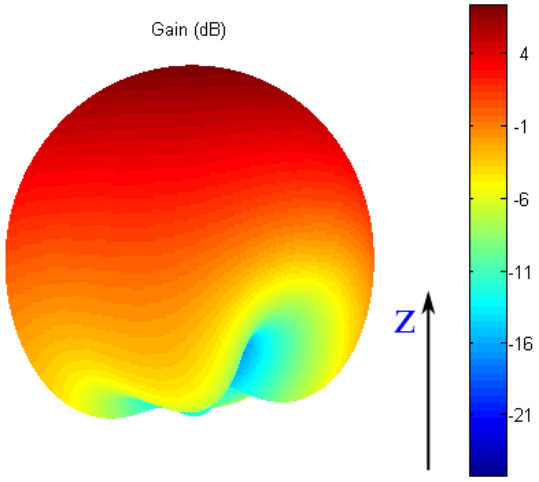

Figure 13: Directivity plotted for the $5.8GHz$ rectangular patch antenna.

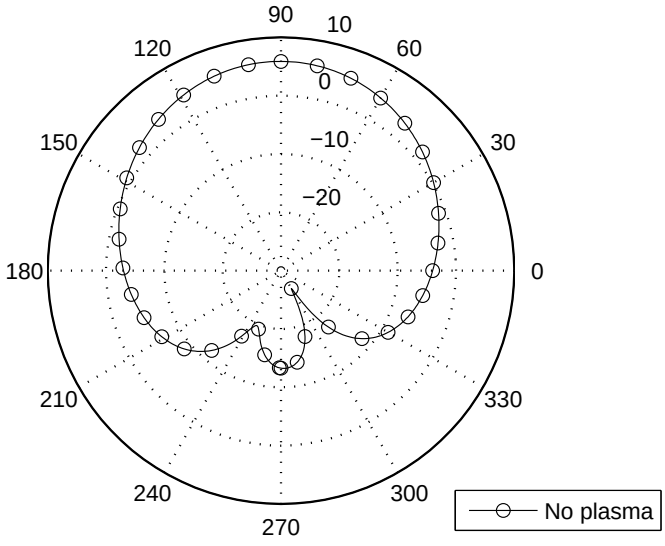

Figure 14: Directivity cross-section plotted for the $5.8GHz$ rectangular patch antenna in the xz-plane, correlated with the antenna geometry as seen in Fig. 12.

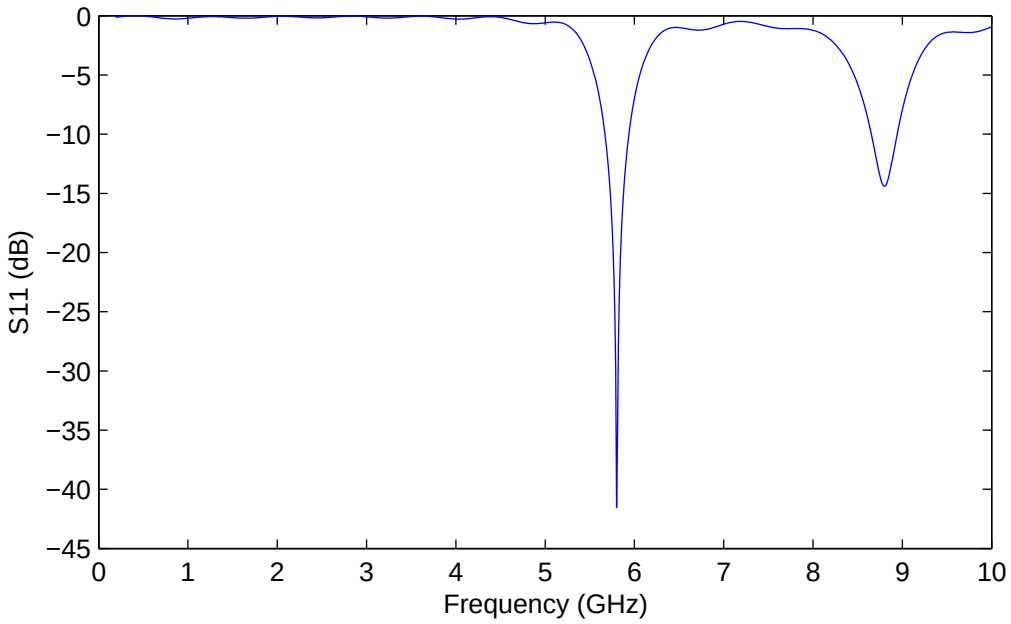

Figure 15: Return loss for the $5.8GHz$ rectangular patch antenna. It shows a minimum return loss at $5.8GHz$ with a $-10dB$ bandwidth of $270MHz$ (4.7%).

gas as frequency goes to infinity, which is 1 for the case of air.

Since a corona is not spatially uniform, it is modeled using discrete slabs, each of whose properties corresponds to a different electron density [31]. First, a simple scenario is considered of a planar patch antenna completely covered in a uniform corona plasma. This scenario is not likely to occur in reality due to the tendency for corona to form around a point where a large electric field magnitude exists. This could occur on the surface of the antenna due to roughness from aging or foreign material buildup such as water or dust. More likely, a corona would form on the corner or edge of the antenna where sharp geometries exist. Predicting exactly where a corona will form on the antenna is not a practical approach to the problem because of the diversity of variable factors which would affect the result. Regardless, it is important to determine how an antenna behaves if it is exposed to a corona plasma, so a layered medium is constructed to emulate a corona formation. Ten layers of rectangular slabs are used in the simulation, as was done in [31]. Drude model parameters are assigned

Figure 16: Depiction of the model of a negative corona with a peak electron density of $n_{e,max} = 10^{19}m^{-3}$. For a negative corona, the electrons at the antenna surface have not attained sufficient energy to initiate an electron avalanche, leading to a low initial electron density. Electron density drops by an order of magnitude for each of the slabs after the peak.

to each slab according to the electron density in that slab.

The electron densities for the slabs are chosen based on the peak electron density in the plasma, and whether it is a positive or a negative corona. The main distinguishing feature in the model of a negative vs. a positive corona is the low electron density at the surface of the antenna in the negative corona. For a negative corona, the electrons being accelerated away from the antenna surface do not have sufficient energy to initiate an electron avalanche initially, leading to a low electron density at the surface. The electron density quickly builds up, with a peak in the second layer. Each successive slab decreases by an order of magnitude. The slab at the surface is taken to have an electron density of $n_e = 10^9 m^{-3}$, from a simulation performed by Chen [22]. This density does not affect the electromagnetic simulation results significantly if it is below $10^{18}m^{-3}$, as explained earlier regarding electromagnetic wave propagation through a plasma.

A table of the plasma frequency vs. electron density is given in Table 4.2. Also provided in Table 4.2 is the distribution of the electron densities for each combination of plasma type (positive or negative) and peak electron density. The layers are arranged over the antenna as shown in Fig. 16, with layer 1 being at the antenna surface and layer 10 being farthest from the surface. The width of each layer extends out to the edge of the antenna substrate, as shown in Fig. 16 and given in Appendix

A.

Table 3: Plasma frequencies corresponding to different electron densities.

$n_e\ (m^{-3})$	10^9	10^{10}	10^{11}	10^{12}	10^{13}	10^{14}
$\omega_p\ (rad/s)$	1.78×10^6	5.64×10^6	1.78×10^7	5.64×10^7	1.78×10^8	5.64×10^8
$n_e\ (m^{-3})$	10^{15}	10^{16}	10^{17}	10^{18}	10^{19}	10^{20}
$\omega_p\ (rad/s)$	1.78×10^9	5.64×10^9	1.78×10^{10}	5.64×10^{10}	1.78×10^{11}	5.64×10^{11}

Table 4: Electron densities used in material layers for each case of positive and negative corona for a given maximum electron density in the corona. Each layer has an equal thickness, given by the total corona thickness divided by 10, the number of layers.

Layer	$n_e(m^{-3})$					
	Negative Corona, $n_{e,max}$			Positive Corona, $n_{e,max}$		
	10^{18}	10^{19}	10^{20}	10^{18}	10^{19}	10^{20}
1 (Antenna Surface)	10^9	10^9	10^9	10^{18}	10^{19}	10^{20}
2	10^{18}	10^{19}	10^{20}	10^{17}	10^{18}	10^{19}
3	10^{17}	10^{18}	10^{19}	10^{16}	10^{17}	10^{18}
4	10^{16}	10^{17}	10^{18}	10^{15}	10^{16}	10^{17}
5	10^{15}	10^{16}	10^{17}	10^{14}	10^{15}	10^{16}
6	10^{14}	10^{15}	10^{16}	10^{13}	10^{14}	10^{15}
7	10^{13}	10^{14}	10^{15}	10^{12}	10^{13}	10^{14}
8	10^{12}	10^{13}	10^{14}	10^{11}	10^{12}	10^{13}
9	10^{11}	10^{12}	10^{13}	10^{10}	10^{11}	10^{12}
10 (Farthest)	10^{10}	10^{11}	10^{12}	10^9	10^{10}	10^{11}

Simulations are performed for the rectangular patch antenna with the plasma Drude material layers as given in Table 4.2 and the results are summarized in the

following section.

4.3 Simulation results

In this section, the results of the simulations are shown through plots comparing the antenna characteristics to the plasma parameters.

The plasma parameters to be varied are:

- Peak electron density, $n_e(m^{-3}) = \{10^{18}, 10^{19}, 10^{20}\}$
- Plasma thickness, $t(mm) = \{0.5, 1.0, 5.0\}$
- Plasma type, {positive,negative}

The peak plasma material setup for the peak electron densities and plasma types are given in Table 4.2. The plasma thickness, t, refers to the total thickness of the plasma materials, as shown in Fig. 16. Therefore, a $1mm$ plasma would indicate that each of the 10 layers has a thickness of $1mm/10 = 0.1mm$.

Throughout the plots, a consistent linestyle is maintained for each plasma variation for easy comparison. Line color, as well as marker orientation, is used to differentiate plasma types. Line marker types are used to differentiate corona thickness. Line style (dashed or continuous) is used to differentiate peak electron density. There is a legend in each figure for reference.

4.3.0.1 Antenna detuning due to corona plasma

The return loss vs. electron density for the $5mm$ thick plasma is shown in Fig. 17. The return loss vs. electron density for the $1.0mm$ thick plasma is shown in Fig. 18. The return loss vs. electron density for the $0.5mm$ thick plasma is shown in Fig. 19. A qualitative analysis of these three figures shows that the return loss increases with both with plasma thickness and plasma density. The resonant frequency of the antenna, here the frequency with the lowest return loss, does not shift significantly

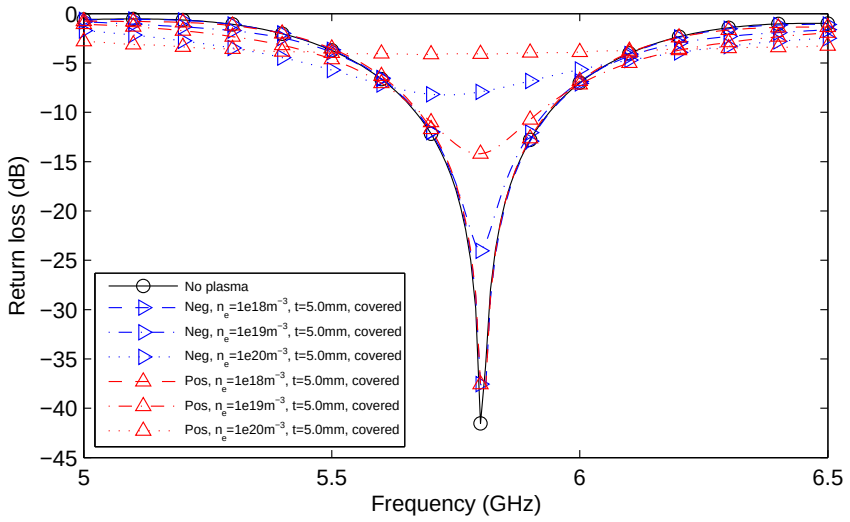

Figure 17: Return loss vs. frequency for the $5.8GHz$ rectangular patch covered in a $5.0mm$ thick corona plasma. The legend indicates the type of corona (positive or negative), peak electron density, plasma thickness, and that the antenna is completely covered with the corona as in Fig. 16.

from the center frequency of $5.8GHz$. The quality factor, Q, of the antenna decreases with electron density. Q is defined for a series RLC circuit in (12).

$$Q = \frac{1}{R}\sqrt{\frac{L}{C}} \tag{12}$$

To understand how Q is increasing, we can look and the input resistance and reactance of the antenna.

The antenna input resistance at the operating frequency of $5.8GHz$ is plotted against the corona peak electron density for the different corona types and thicknesses in Fig. 20. The resulting trend shows that the input resistance increases with peak electron density. The input resistance of the antenna around resonance can be interpreted as the series combination of the radiation resistance and a resistance representing energy dissipated in the antenna as heat [32]. The increase in the input resistance, then, makes sense, since the energy dissipated in the antenna increases with electron density. Here, we are treating the plasma as a lossy dielectric which is a part of the antenna. We can now see that the quality factor, Q, of the antenna (12)

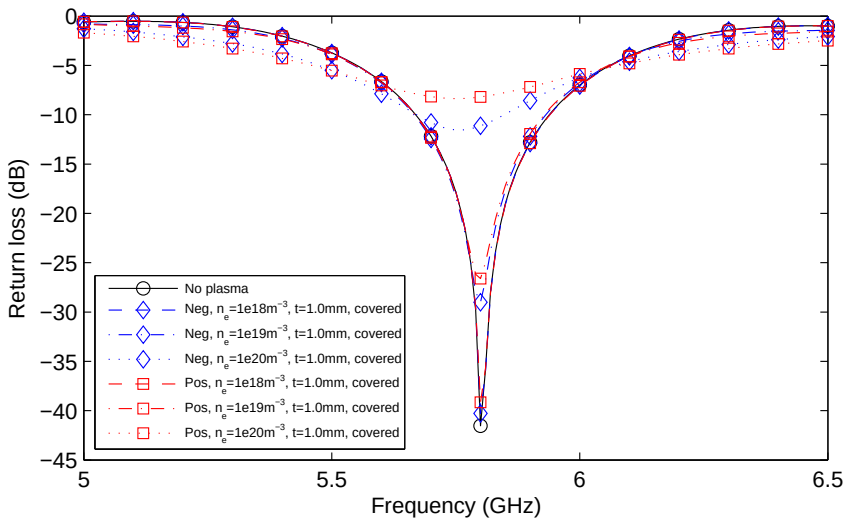

Figure 18: Return loss vs. frequency for the $5.8GHz$ rectangular patch covered in a $1.0mm$ thick corona plasma. The legend indicates the type of corona (positive or negative), peak electron density, plasma thickness, and that the antenna is completely covered with the corona as in Fig. 16.

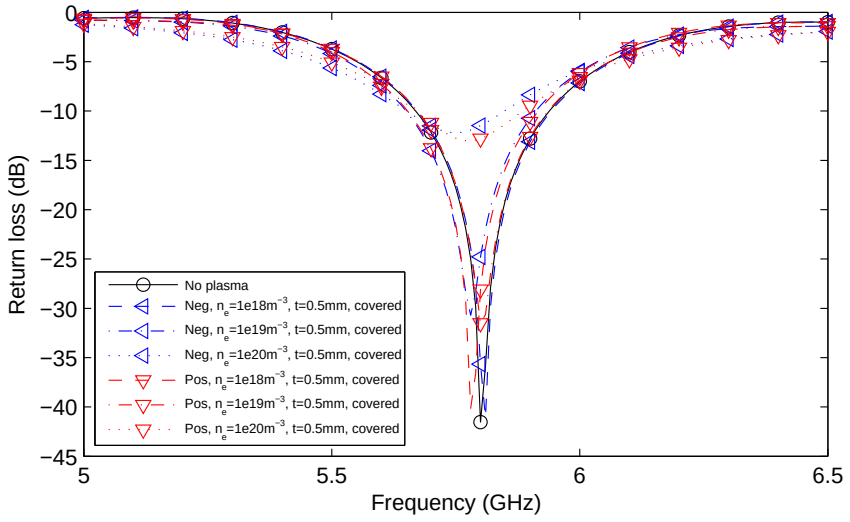

Figure 19: Return loss vs. frequency for the $5.8GHz$ rectangular patch covered in a $0.5mm$ thick corona plasma. The legend indicates the type of corona (positive or negative), peak electron density, plasma thickness, and that the antenna is completely covered by the corona as in Fig. 16.

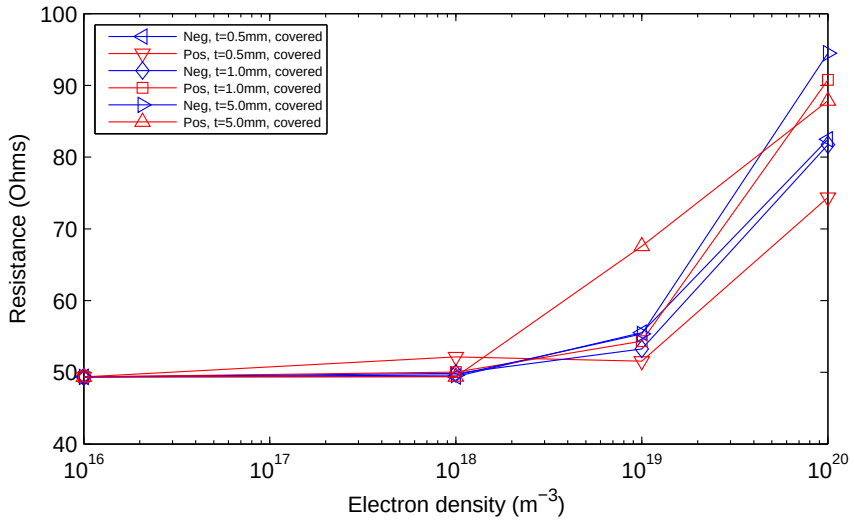

Figure 20: Antenna input resistance vs. corona peak electron density at $5.8GHz$ for the rectangular patch antenna. The legend indicates the type of corona (positive or negative), plasma thickness, and that the antenna is completely covered by the corona as in Fig. 16. The resistance at a density of $n_e = 10^{16}$ is actually for the case for no plasma, $n_e = 0$, plotted here for shorter x-axis scaling.

increases largely due to the increase in the input resistance.

The antenna input reactance at the operating frequency of $5.8GHz$ is plotted against the corona peak electron density for the different corona types and thicknesses in Fig. 21. The resulting trend shows that the input reactance decreases with peak electron density. This indicates an electric field storage in the antenna. The negative reactance means that the antenna and plasma are acting as a capacitor. The large conducting layer of plasma over the dielectric essentially creates a capacitor, where the electric field energy is stored between the plasma and ground plane in the dielectric.

If an antenna is transmitting, the return loss indicates what proportion of the power available from a signal generator is accepted by the antenna. A return loss of $0dB$ would indicate that all the power from the generator is being reflected away from the antenna and none of the power is being dissipated or radiated. Conversely, a return loss of $-40dB$ or lower indicates that almost all the power available from the generator is being dissipated or radiated by the antenna. We now see that the

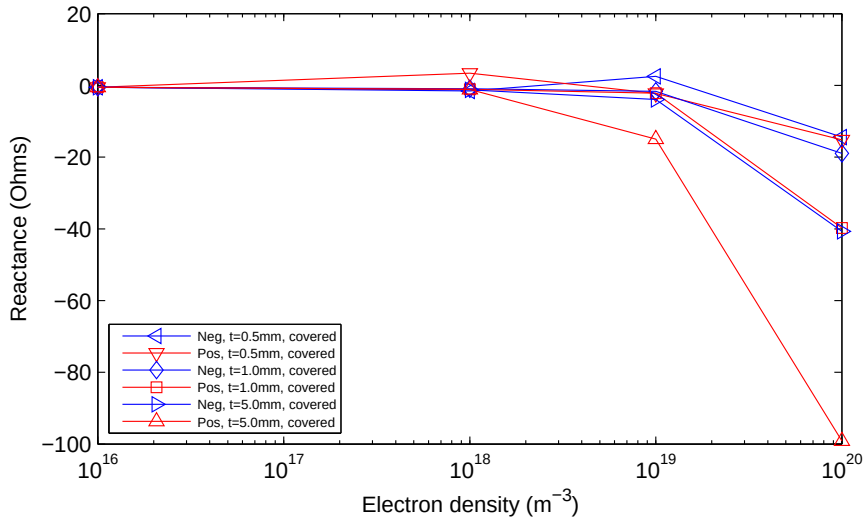

Figure 21: Antenna input reactance vs. corona peak electron density at $5.8GHz$ for the rectangular patch antenna. The legend indicates the type of corona (positive or negative), plasma thickness, and that the antenna is completely covered by the corona as in Fig. 16. The reactance at a density of $n_e = 10^{16}$ is actually for the case for no plasma, $n_e = 0$, plotted here for shorter x-axis scaling.

formation of a corona over the surface of a patch antenna can increase the return loss, indicating that not as much power is being accepted by the antenna. Now we look at what proportion of the power that is accepted by the antenna is actually radiated, and what fraction is lost to the plasma.

4.3.0.2 Antenna signal attenuation due to corona plasma

As discussed earlier in the section on antenna basics, the radiation efficiency, η_{rad}, is the proportion of the power radiated by an antenna to the power accepted by the antenna. The radiation efficiency can be obtained through simulation using CST Microwave Studio. Fig. 22 shows the radiation efficiency of the rectangular patch antenna at $5.8GHz$ as a function of the peak electron density of the corona. The plot illustrates the dramatic increase in attenuation from $n_e = 10^{18}m^{-3}$ to $n_e = 10^{20}m^{-3}$. As with the antenna detuning, attenuation by the plasma does not affect the performance of the antenna until densities on the order of $n_e = 10^{19}m^{-3}$ or higher

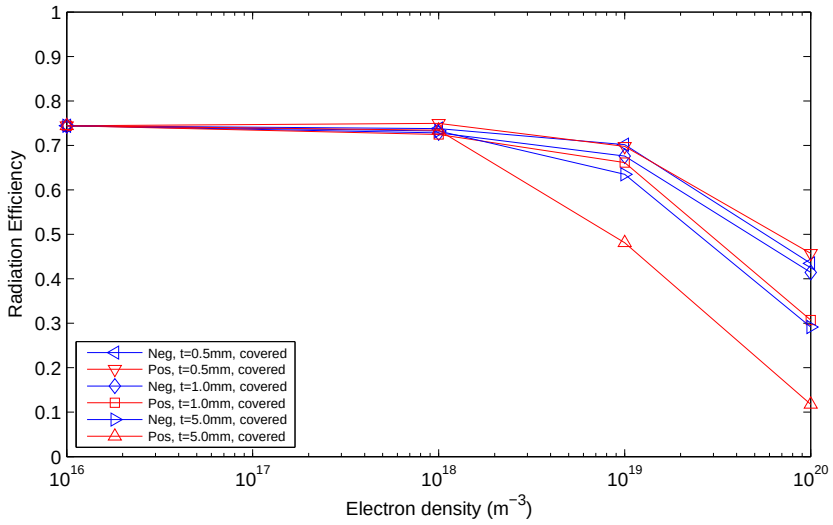

Figure 22: Radiation efficiency vs. peak electron density at $5.8GHz$ for the rectangular patch antenna. The legend indicates the type of corona (positive or negative), plasma thickness, and that the antenna is completely covered by the corona as in Fig. 16. The radiation efficiency at a density of $n_e = 10^{16}$ is actually for the case for no plasma, $n_e = 0$, plotted here for shorter x-axis scaling.

are reached, irrespective of the plasma thickness.

Combining knowledge of the return loss and radiation efficiency, one can obtain a plot of where the power is going in these different corona situations during RF transmission. Fig. 23 is a stacked bar graph for each of the examined corona scenarios. The graph utilizes the conservation of power to show what proportion of power is radiated, lost, and reflected at the antenna port relative to the power available from the generator. The y-axis is normalized to the power available from the generator, P_{av}. Each bar, or column, shows the total power in the antenna transmission system, which sums to the available power. The bar is then divided into four fractional components:

1. P_{rad}: The power radiated by the antenna. This is the quantity of interest which needs to be maximized for optimal operation. Note: This does not incorporate the possible change in antenna directivity as this quantity is extremely

dependent on the corona geometry, which is unknown.

2. P_{refl}: The power reflected at the antenna port back to the generator.

3. $P_{L,ant}$: The power dissipated by lossy materials in the antenna (FR4 and copper). This ratio of $P_{L,ant}$ to P_{acc}, the power accepted into the antenna, is assumed constant as plasma is added to the model.

4. $P_{L,plasma}$: The power dissipated by the plasma.

Under each bar is the exponent of 10 representing the electron density in m^{-3}, i.e. $18 \rightarrow n_e = 10^{18} m^{-3}$. The bars are grouped by plasma thickness, which is subdivided into positive and negative corona.

An additional explanation is needed on how these individual terms are obtained. CST Microwave Studio is capable of performing a full-wave electromagnetic simulation of the antenna and plasma, generating a file containing the available power, P_{av}, accepted power into the antenna, P_{acc}, and radiated power, P_{rad}. The sources of power loss can then be enumerated as follows.

1. P_{rad}: The radiated power is obtained directly, necessitating only a normalization by P_{av}.

2. P_{refl}: The power reflected at the antenna port is obtained by $P_{refl} = P_{av} - P_{acc}$ and normalized by P_{av}.

3. $P_{L,ant}$: In order to differentiate the power lost in the antenna from the power dissipated in the plasma, it is assumed that $P_{L,ant}$ remains directly proportional to the power accepted by the antenna. Since the excited mode of the antenna with and without the plasma is seen to be the same, the losses in the antenna should scale proportionately with the power accepted by the antenna. The relative power lost in the antenna without a plasma is obtained through simulation,

$(P_{acc,0} - P_{rad,0})/P_{acc,0}$, multiplied by the accepted power with a plasma, P_{acc}, and normalized by P_{av}.

4. $P_{L,plasma}$: The power dissipated by the plasma is all power accepted by the antenna that is not lost in the antenna as defined above and not radiated or reflected. Due to the assumption that the relative power lost in the antenna structure is constant, it may be more accurate to state that the power lost to the plasma is really the power dissipated in the *antenna and plasma* above the level of power which would be dissipated in the antenna (and plasma) with no plasma present.

From Fig. 23, it is observed that power attenuation by the plasma is the dominant cause of a decrease in radiated power, as compared with reflection at the antenna port.

While Fig. 23 provides a qualitative means of analyzing the decrease in radiated power, the same values for reflected and plasma dissipated power can be given as losses, in dB. The power loss due to reflection at the antenna port is given in Fig. 24, and the power loss due to plasma absorption is given in Fig. 25.

A comparison of Fig. 25 with Fig. 10 for the case of $n_e = 10^{20} m^{-3}$ shows close agreement for the loss due to the plasma. From Fig. 25, the plasma loss for $1mm$ total thickness is roughly $2-3dB$. From Fig. 10, the attenuation is $20dB/cm$, or $2dB/mm$. While the near field development surrounding the antenna cannot be substituted with a simple plane wave propagation model, the attenuation by the plasma can be obtained by this simple approximation to an order of magnitude. It should be noted that the plane wave approximation in fact underestimates the measured attenuation, since the total thickness of the plasma at the peak electron density constitutes only a portion of the total thickness, as given in Table 4.2.

In order to minimize the power lost due to corona on an antenna, it may be possible to decrease the reflected losses due to an impedance shift. In the next section, a wideband rectangular patch antenna is designed and simulated with corona plasma.

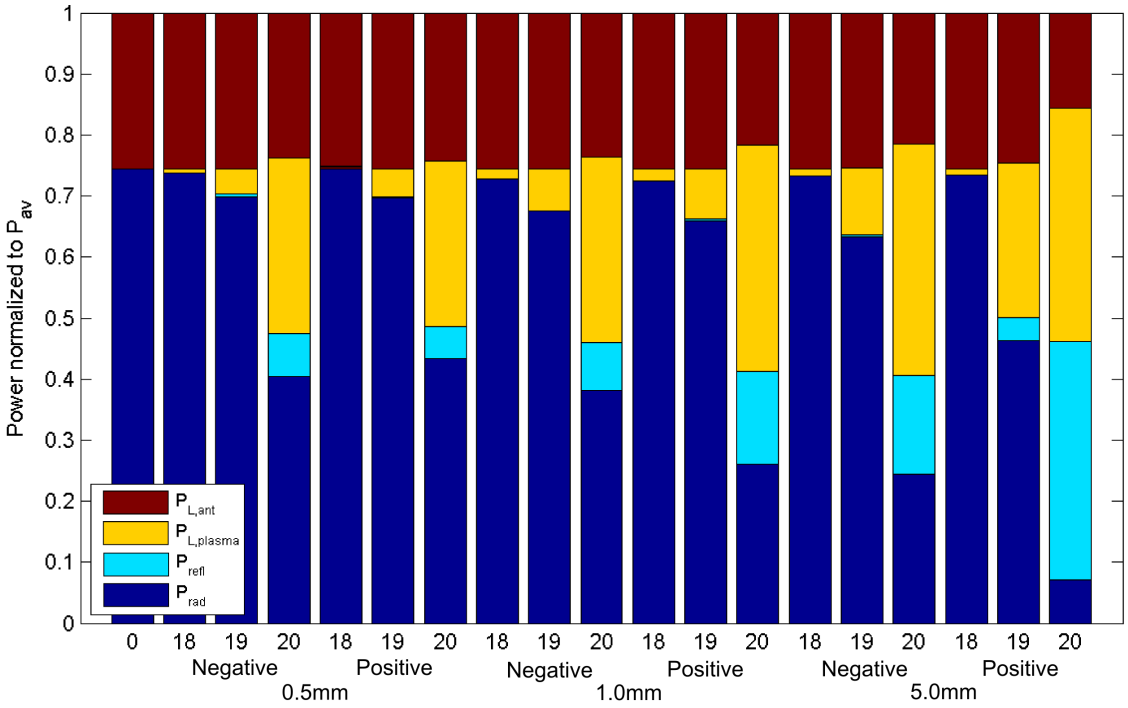

Figure 23: Conservation of available power to the antenna, showing what proportion of the available power from the generator is radiated, reflected, or lost. The x-axis is grouped by plasma thickness, and then plasma type, and finally into the electron density, where the value shown under the bar is the exponent to which 10 is raised to obtain the density in m^{-3}.

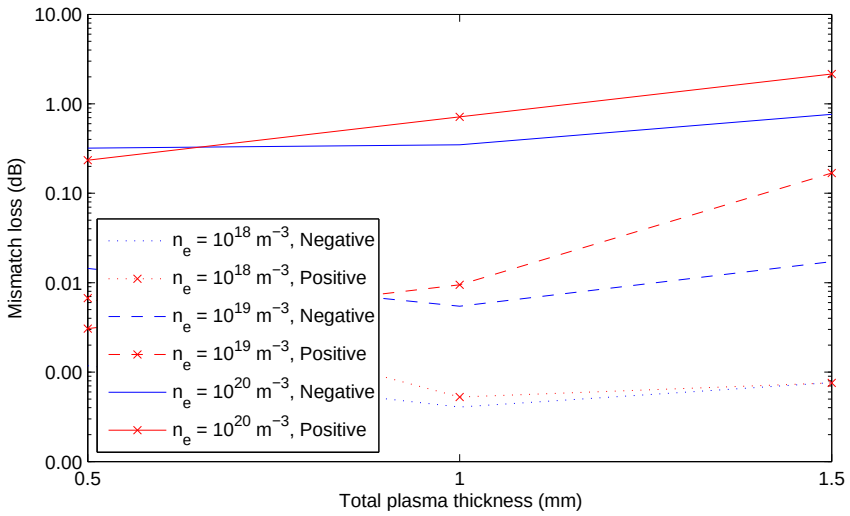

Figure 24: Plot showing the power reflected at the coaxially fed rectangular patch antenna port as a function of plasma thickness. Plots are given for both positive and negative corona variations and for different peak electron densities. The power reflected at the port, or mismatch loss, is given by $10 \log_{10} P_{av}/P_{acc}$ and is different from the commonly quoted return loss.

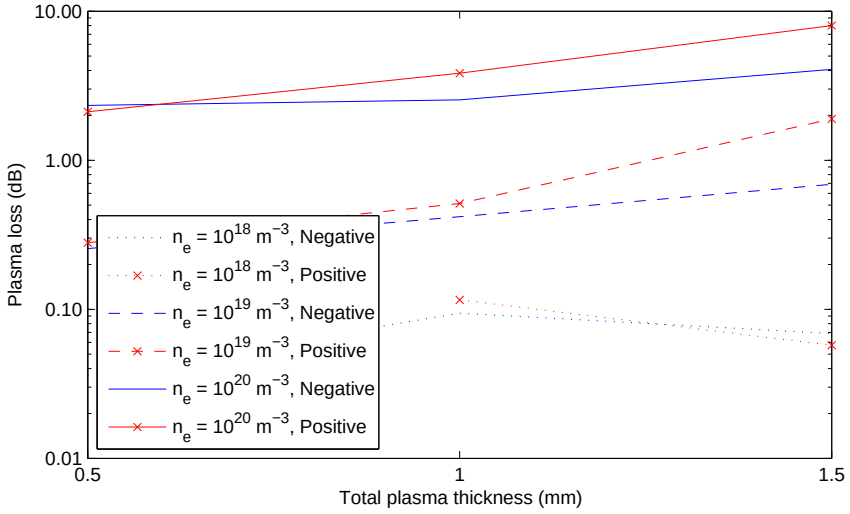

Figure 25: Plot showing the power lost, or absorbed, due to the plasma on the rectangular antenna surface. Plots are given for both positive and negative corona variations and for different peak electron densities.

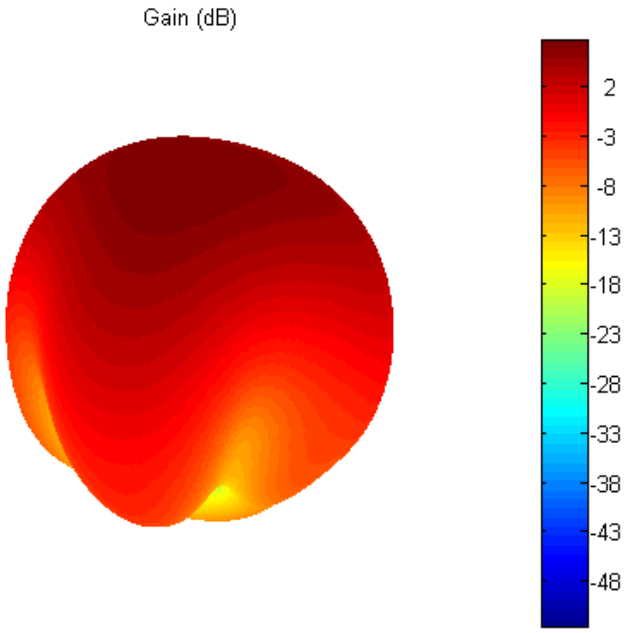

Figure 26: Directivity plotted for the wideband 5.8GHz E-shaped rectangular patch antenna.

4.4 Comparison with wideband rectangular patch performance

A coaxially fed wideband E-shaped rectangular patch is designed and simulated in CST Microwave Studio from [33]. The patch is again designed to operate at 5.8GHz and is created on the same lossy FR4 substrate with copper. A top view of the patch is shown in Fig. 38 in Appendix A. This figure replaces Fig. 37 in Appendix A for diagramatic purposes, but the dimension labels used in Figs. 39,40,41 in the Appendix are still valid for the wideband patch. The dimensions of the wideband rectangular patch are given in Table A in units of mm.

The directivity of the wideband patch antenna is plotted in Figs. 26-27. The return loss of the antenna is plotted in Fig. 28 referenced to 50Ω. The characteristics of the patch antenna are given in Table 4.4.

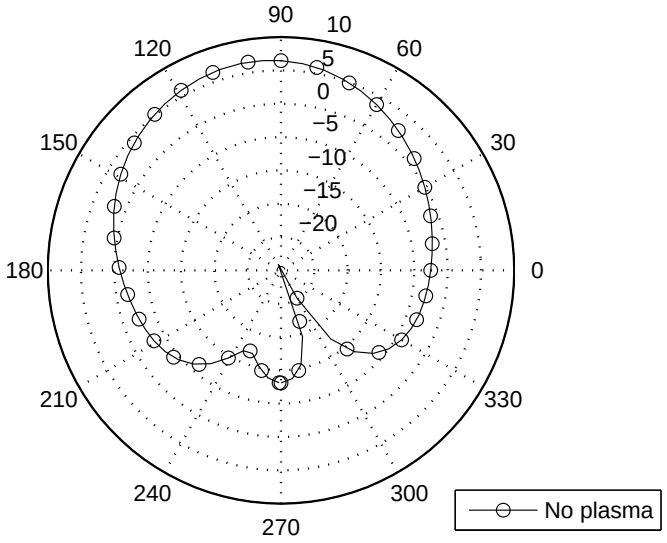

Figure 27: Directivity cross-section plotted for the wideband $5.8GHz$ E-shaped rectangular patch antenna in the xz-plane.

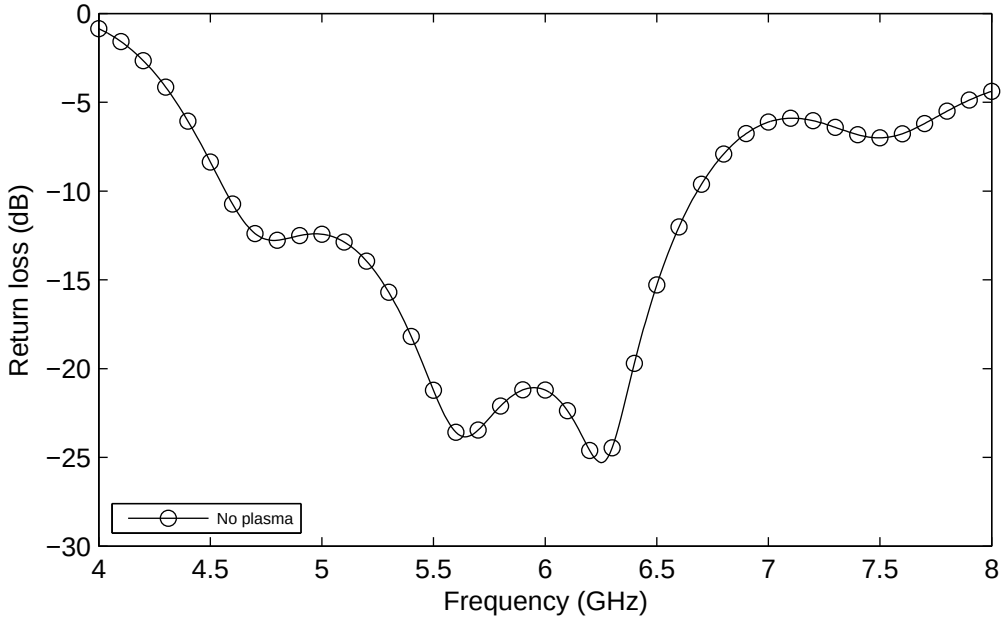

Figure 28: Return loss for the wideband $5.8GHz$ E-shaped rectangular patch antenna. It shows a wide $-10dB$ bandwidth of $2.11GHz$ (36.4%).

Table 5: Simulated characteristics of the wideband $5.8GHz$ E-shaped rectangular patch antenna from CST Microwave Studio.

Parameter	Value	Units
Frequency	5.8	GHz
Directivity	6.62	dBi
Gain	6.31	dBi
Radiation Efficiency	93.1	%
$-10dB$ Bandwidth	36.4	%
Input Impedance	$57.9 - 3.09i$	Ω

Similar to the rectangular patch, the wideband patch is subjected to corona and its radiation characteristics are assessed. The same layered model for a plasma material is utilized as given in Table 4.2. Fig. 29 shows the return loss vs. frequency for the wideband patch with a $5.0mm$ plasma of varying electron densities. This plasma showed the most detuning of the rectangular patch, as seen by the large proportion of power lost due to reflection, P_{refl} in Fig. 23. The return loss for the wideband patch in this configuration is shown in Fig. 29, and can be compared with the return loss for the rectangular patch in Fig. 17. The wideband patch is able to maintain a return loss under $-10dB$ even when subjected to the $5.0mm$ thick corona plasma with a peak electron density of $10^{20}m^{-3}$. Under these same circumstances, the rectangular patch's return loss fell to $-4dB$ at its operating frequency of $5.8GHz$.

As with the rectangular patch, the wideband patch is examined in terms of energy conservation. Fig. 32 is a stacked bar graph for each of the examined corona scenarios. The graph utilizes the conservation of energy to show what proportion of power is radiated, lost, and reflected relative to the power available from the generator. The y-axis is normalized by the power available from the generator, P_{av}. Each bar, or column, shows the total power in the antenna transmission system, which sums to

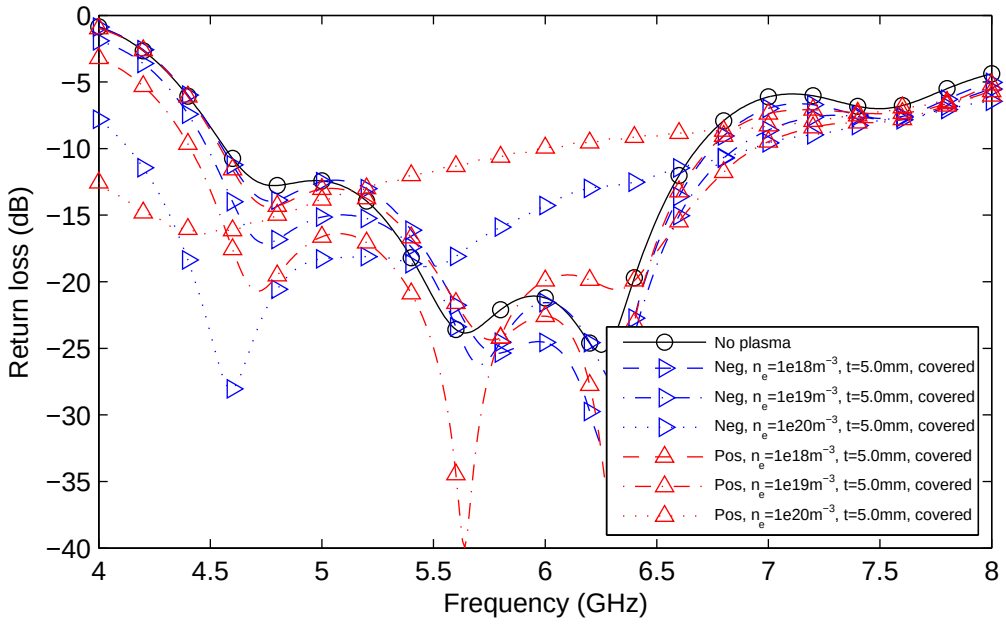

Figure 29: Return loss vs. frequency for the wideband $5.8GHz$ E-shaped rectangular patch covered in a $5.0mm$ thick corona plasma. The legend indicates the type of corona (positive or negative), peak electron density, plasma thickness, and that the antenna is completely covered with the corona as in Fig. 16.

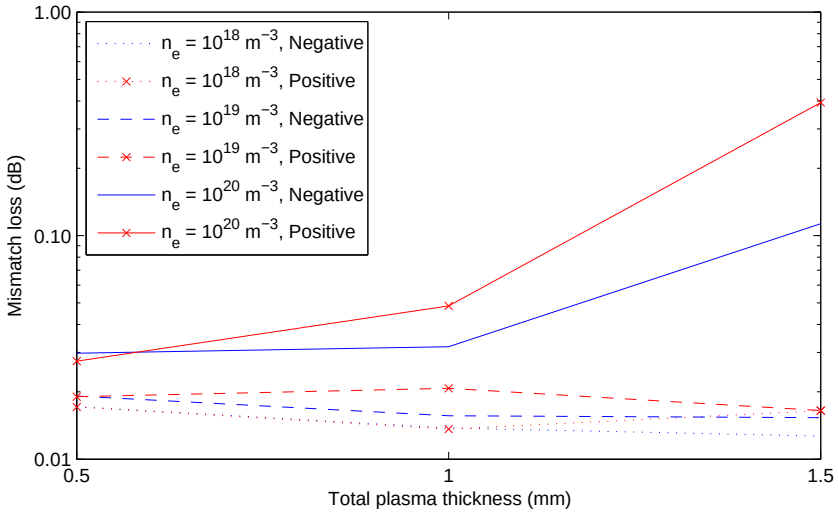

Figure 30: Plot showing the power reflected at the coaxially fed wideband patch antenna port as a function of plasma thickness. Plots are given for both positive and negative corona variations and for different peak electron densities. The power reflected at the port, or mismatch loss, is given by $10 \log_{10} P_{av}/P_{acc}$ and is different from the commonly quoted return loss.

the available power. All powers are normalized by the available power from the generator, P_{av}.

After analyzing Fig. 32, it is evident that power attenuation by the plasma is again the primary cause of a decrease in radiated power. The reflected power lost due to antenna detuning constitutes less than 10% of the total power loss in the worst case. The wideband antenna is resilient against detuning due to plasma formation, but attenuation due to plasma is still the bigger issue. The radiated power from the wideband patch antenna is on the order of the rectangular patch antenna, and little improvement is actually seen, comparing Figs. 32 and 23.

Again, the values for reflected and plasma dissipated power can be given as losses, in dB. The power loss due to reflection at the antenna port is given in Fig. 30, and the power loss due to plasma absorption is given in Fig. 31.

A comparison of Fig. 31 with Fig. 25 shows close agreement for the loss due to the plasma. The resonance of the antenna has little impact on the attenuation by the

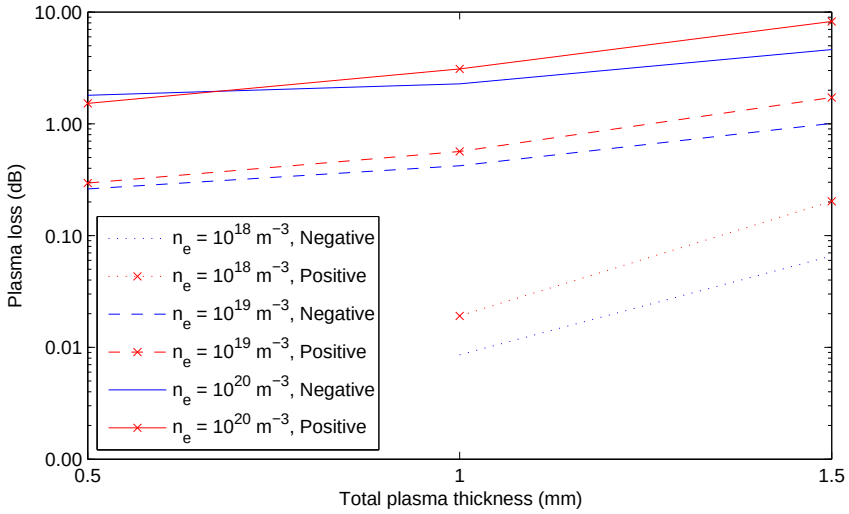

Figure 31: Plot showing the power lost, or absorbed, due to the plasma on the wideband antenna surface. Plots are given for both positive and negative corona variations and for different peak electron densities.

plasma. However, the mismatch loss is affected by the resonance of the antenna. In Fig. 24, the mismatch loss increases from nearly $0dB$ in the low plasma density case to $2dB$ in the worst case. The wideband patch antenna, shown in Fig. 30, reaches a peak mismatch loss of $0.4dB$, a difference of $1.5dB$ from the rectangular patch. While the rectangular patch antenna can match the feed impedance closer in a free space scenario, it's high Q makes it vulnerable to detuning.

Nevertheless, the studies conducted in these two sections present an extreme case of corona formation where the entire antenna is enveloped by the plasma. In reality, corona are likely to form at small points such as corners or edges of the antenna. The following section evaluates the effect on a small point corona formation on the rectangular patch antenna.

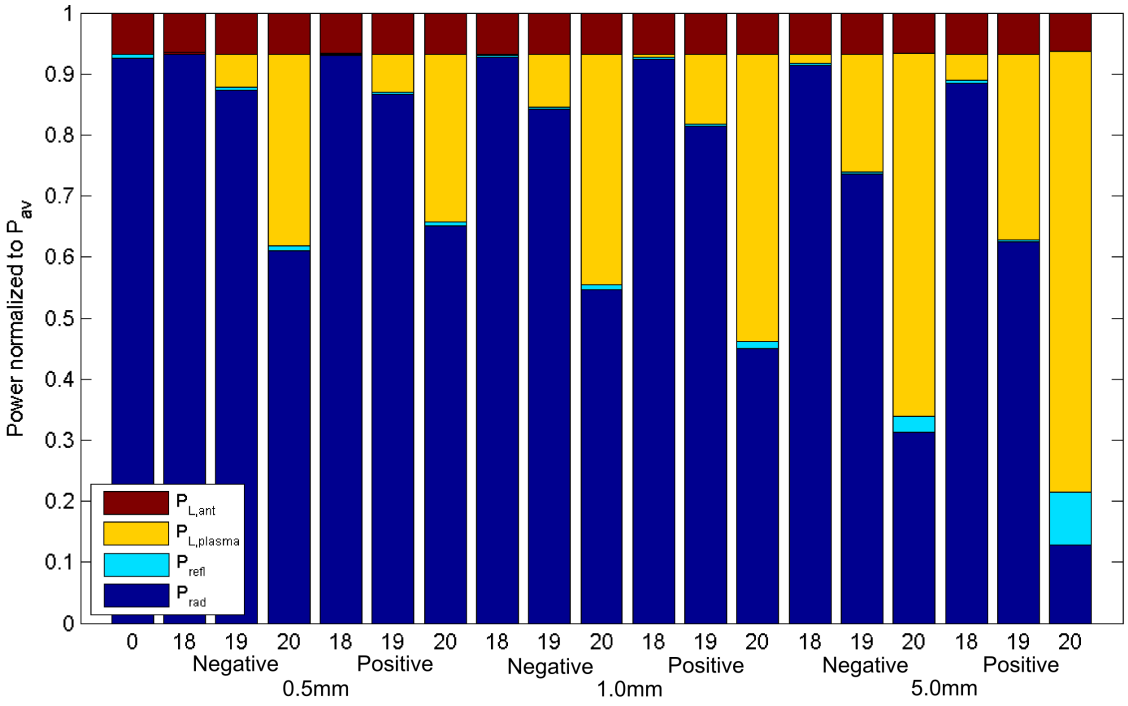

Figure 32: Conservation of available power to the wideband patch antenna, showing what proportion of the available power from the generator is radiated, reflected, or lost. The x-axis is grouped by plasma thickness, and then plasma type, and finally into the electron density, where the value shown under the bar is the exponent to which 10 is raised to obtain the density in m^{-3}.

4.5 Evaluation of patch antenna performance in point corona

The previous two sections have evaluated the performance of a patch antenna when completely enveloped by a corona plasma on the face of the patch. This section studies the effect on a small point corona on the patch. Fig. 33 shows the form that a negative point corona takes on a small point. The corona in the drawing taken from Loeb [1, p.520] illustrates how a corona spreads in space, with decreasing electron density as the corona gets further from the point. The corona in this figure has an extent of $1.5mm$. In the figure, the dark space is also visible where there

is a gap between the point and the visible plasma due to low electron energies as they accelerate away from the surface. The figure is useful in illustrating the general shape of the corona. From this, a model is made in CST Microwave Studio of a point corona at the edge of the $5.8GHz$ rectangular patch antenna. The corona is modeled as an inverted cone with a flattened tip, depicted in Fig. 34. The radius of the tip in contact with the edge of the antenna is $0.5mm$. The same 10 layer model is used for the corona electron densities as in earlier simulations. The radius of the cone at the top of the tenth layer is equal to the thickness of the corona, t, plus $0.5mm$. The tip of the corona is situated halfway overlapping the antenna. A diagramatic cross section of the point corona model used is shown in Fig. 35.

The power conservation analysis is performed on the rectangular patch in the spot corona, and the results are shown in Fig. 36. The graph utilizes the conservation of energy to show what proportion of power is radiated, lost, and reflected back to the generator relative to the power available from the generator. The y-axis is the power available from the generator, P_{av}, normalized by itself, resulting in 1. Each bar, or column, shows the total power in the antenna system, which sums to the available power. The results show that antenna detuning due to a localized point corona on a patch is not an issue. Some power loss due to absorption in the plasma is seem. However, this represents a negligible ($\sim 0.3dB$) drop in signal power. With this said, isolated point corona phenomena on the planar patch antenna do not pose a serious threat to a communication system.

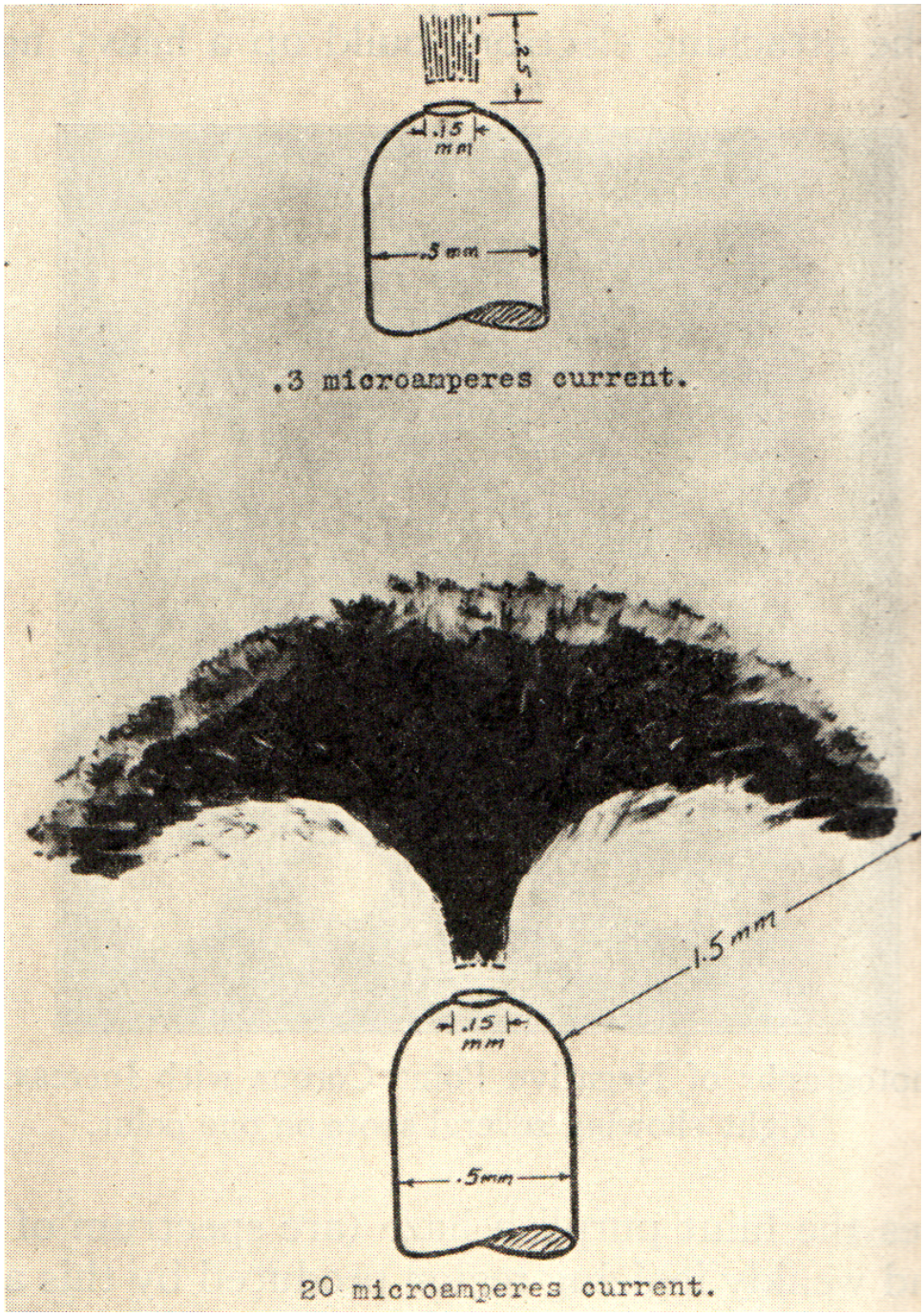

Figure 33: Hand drawing of a negative point corona [1, p.520].

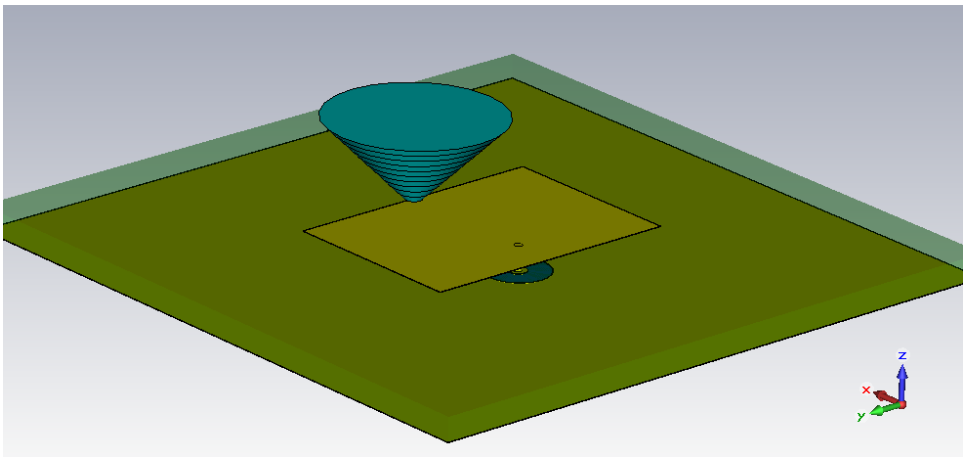

Figure 34: Screenshot from CST Microwave Studio of the point corona at the edge of the $5.8GHz$ rectangular patch. An inverted cone model is used with a flattened tip at the antenna surface. The cone is split into uniformly thick layers as in previous simulations.

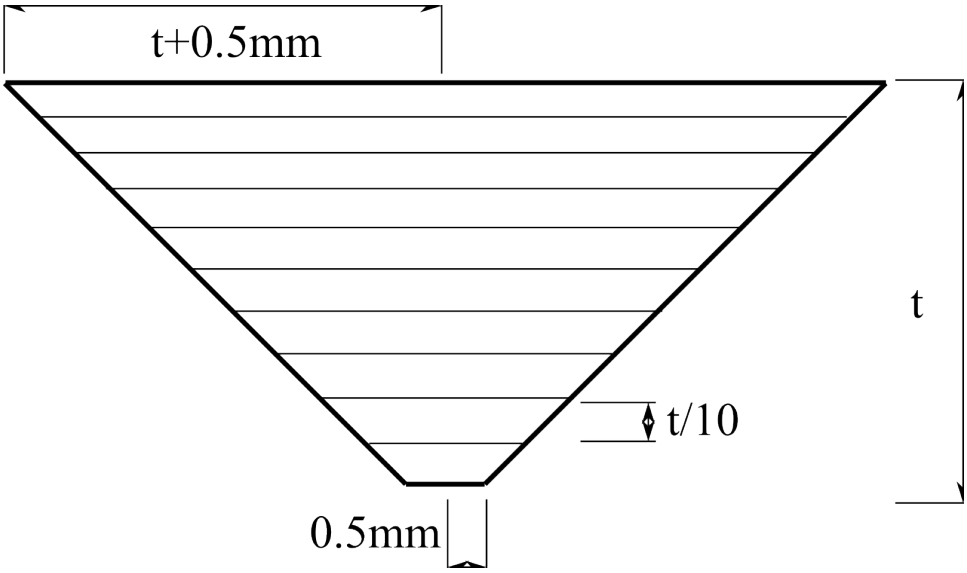

Figure 35: Cross section of the point corona cone. The $0.5mm$ tip of the corona is in contact with the surface of the antenna. The first layer at the tip corresponds to layer 1 from Table 4.2. t is the thickness of the corona used in simulation, either 0.5, 1.0, or $5.0mm$.

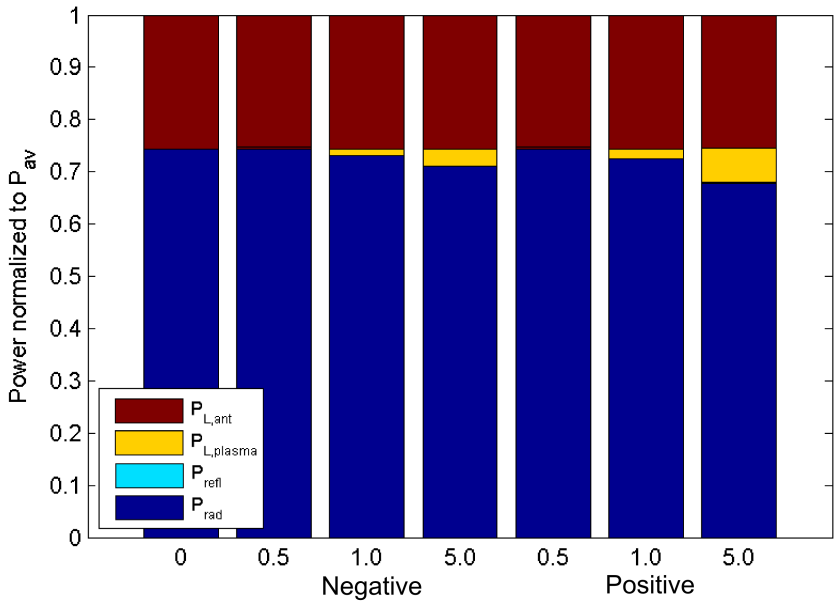

Figure 36: Conservation of available power to the antenna, showing what proportion of the available power from the generator is radiated, reflected, or lost. The x-axis is grouped by plasma type into three Negative and three Positive point corona simulations, and finally into the plasma thickness (mm). All simulations are shown for the plasma distribution with a peak electron density of $10^{20}m^{-3}$.

CHAPTER V

CONCLUSION AND FUTURE WORK

The effect of a high-voltage corona plasma on a planar patch antenna has been evaluated. The formation of corona plasma on an antenna at high-voltage poses a threat to the antenna's ability to communicate. The potential for corona formation on an antenna exists if the electric field intensity is high enough at its surface. The exact criteria for corona formation depend strongly on the environment (weather, temperature, pollution in the air, etc.) and the geometry of the antenna and its surroundings. However, approximations can be made for corona onset conditions. Using Peek's law affords the ability to predict visible corona onset between two parallel wires, or between a wire and a ground plane, with a large electric potential between them. A simple rule of thumb is to avoid geometries where the electric field at any point exceeds $30kV/cm$, which is the approximate disruptive critical gradient, or dielectric strength, for air. Since the electric field intensity increases with the "sharpness" of a point or corner, corona will tend to form at corners and points. Therefore, in antenna design it is important to keep the geometry round or flat. A planar antenna affords a convenient solution to the issue of minimizing electric field intensity at the antenna surface when it is at a high electric potential.

A treatment of the corona plasma using the Drude dispersive model allows for electromagnetic simulations of an antenna in the presence of a corona. The Drude model, through the use of a physical understanding of free electron motion in a plasma, is able to relate plasma properties such as electron density and collision frequency to a complex permittivity. The free electrons in a corona act as a poor conductive medium, causing an attenuation of an electromagnetic wave passing through it. At atmospheric

pressure, the electrons absorb the energy of an electromagnetic wave passing through them, and dissipate that energy as thermal energy through collisions with neutral molecules. At atmospheric pressure, the collision frequency is high enough that the plasma behavior varies significantly from a low-pressure plasma. In an atmospheric pressure plasma, it is beneficial to utilize lower electromagnetic wave frequencies to minimize attenuation through the plasma. At UHF and microwave frequencies, the attenuation (db/cm) increases roughly proportionally to $\sqrt{f}$. Attenuation is also roughly proportional to electron density in this region.

A planar antenna with a corona buildup on its surface will not only lose its energy through attenuation in the plasma, the antenna will also detune due to the proximity of the conductive medium. Using CST Microwave Studio, simulations are performed for the behavior of a $5.8GHz$ rectangular patch antenna whose surface is completely covered by a corona plasma. The simulations vary the plasma electron densities, plasma thickness, and corona type (positive and negative). The primary difference between the positive and negative corona is the low electron density region right at the surface of the antenna in the negative corona. The results show that the narrowband patch both detunes and loses energy to absorption in the plasma. Even with the narrowband patch, absorption by the plasma is the dominant source for loss of radiated power. The same simulations are also performed for a wideband patch antenna at $5.8GHz$. The wideband patch shows resilience against detuning. However, severe signal attenuation occures for high electron densities as well. Both patches exhibited signal power loss on the order of $10dB$ when covered in a corona with a peak electron density of $10^{20}m^{-3}$. In reality, a corona will not envelop the entire antenna, so simulations are performed to show the effect of a point corona on the edge of the $5.8GHz$ rectangular patch antenna. The results show that a point corona has minimal effect on the antenna performance. There is practically no detuning and signal power loss less than $1dB$.

In a system implementation, it would be beneficial to utilize a wideband patch or other planar antenna in order to minimize the losses due to detuning, regardless of the possible losses due to plasma attenuation. It would also be good practice to incorporate a $10dB$ or higher link margin in the system design in the event of a large corona formation on the antenna.

There is much opportunity for future work in this area to improve the understanding of corona effects on antennas. Simulations can be performed for antennas of various frequencies to see how they perform compared with each other. In addition, different types of antennas can be experimented with to see how the resonant mode and near field formation affects the attenuation by the plasma. Such antennas might include slot and printed dipole antennas. The effects of magnetic fields, such as those generated by large currents in the power line, on corona formation should also be investigated. In addition, the possible use of static magnetic fields for corona mitigation can be investigated as a way to minimize signal attenuation [28].

APPENDIX A

RECTANGULAR AND WIDEBAND PATCH ANTENNA DESIGN

The dielectric substrate used for the patch antennas (shown in green in Fig. 12 is FR4 with a relative permittivity of $\varepsilon_{r,FR4} = 4.1$ and a dielectric loss tangent of $tan\delta_{FR4} = 0.016@1GHz$. The insulator for the coaxial feed line is PTFE with a relative premittivity of $\varepsilon_{r,PTFE} = 2.1$ and a loss tangent of $tan\delta_{PTFE} = 0$.

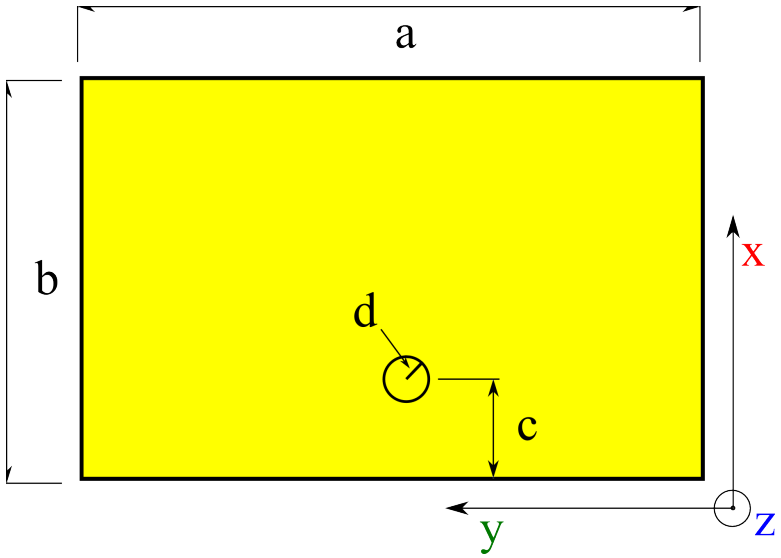

Figure 37: Top view of the $5.8GHz$ rectangular patch antenna. The yellow material represents copper. The ground plane and FR4 dielectric substrate are not depicted in this figure. The antenna is symmetric across the xz-plane.

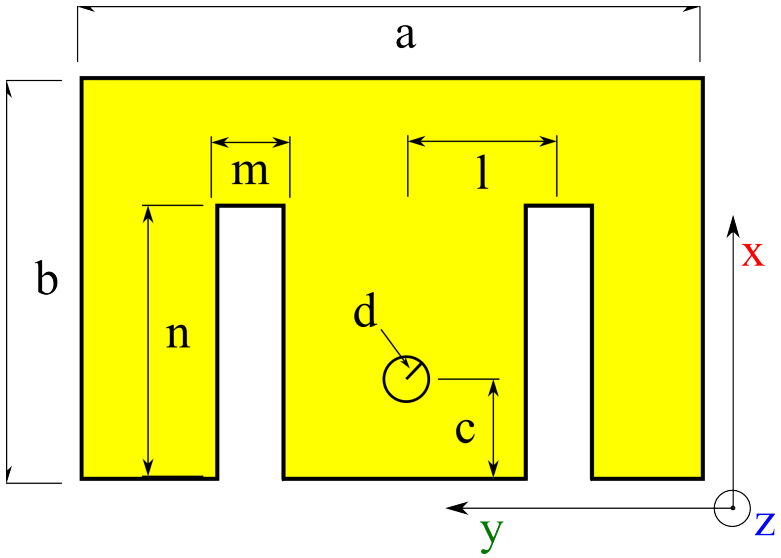

Figure 38: Top view of the wideband $5.8GHz$ E-shaped rectangular patch antenna. The yellow material represents copper. The ground plane and FR4 dielectric substrate are not depicted in this figure. The antenna has two slots cut into it and is symmetric across the xz-plane.

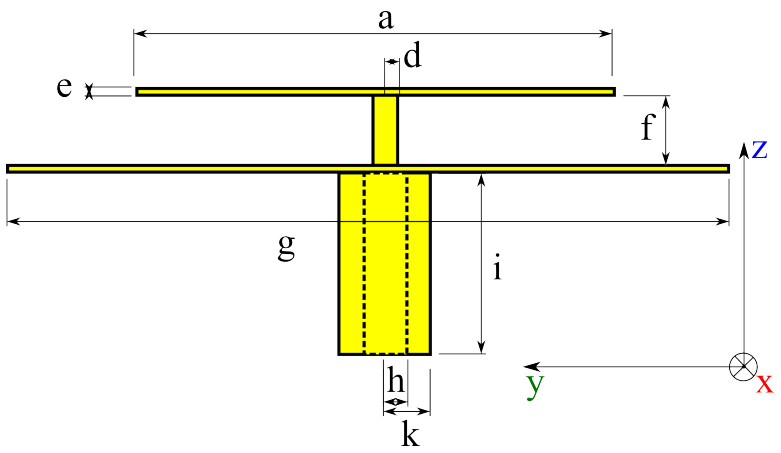

Figure 39: Front view of $5.8GHz$ wideband and regular rectangular patch antennas. The yellow material represents copper. The dotted line represents an inner coaxial conductor that is inside the outer conductor shown. The FR4 dielectric substreate is not depicted in this figure.

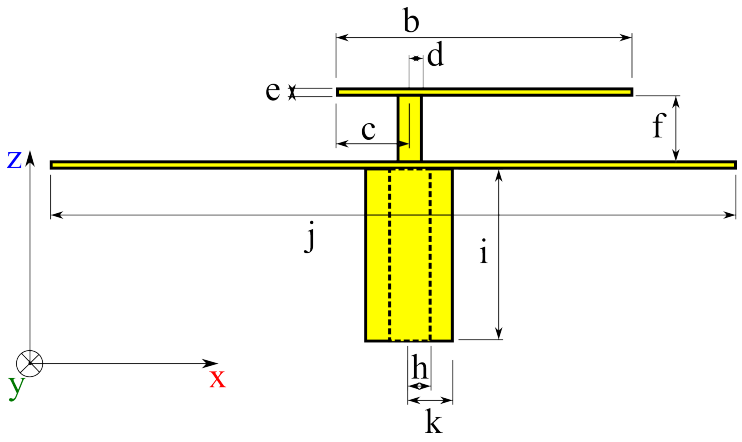

Figure 40: Side view of $5.8GHz$ wideband and regular rectangular patch antennas. The yellow material represents copper. The dotted line represents an inner coaxial conductor that is inside the outer conductor shown. The FR4 dielectric substreate is not depicted in this figure.

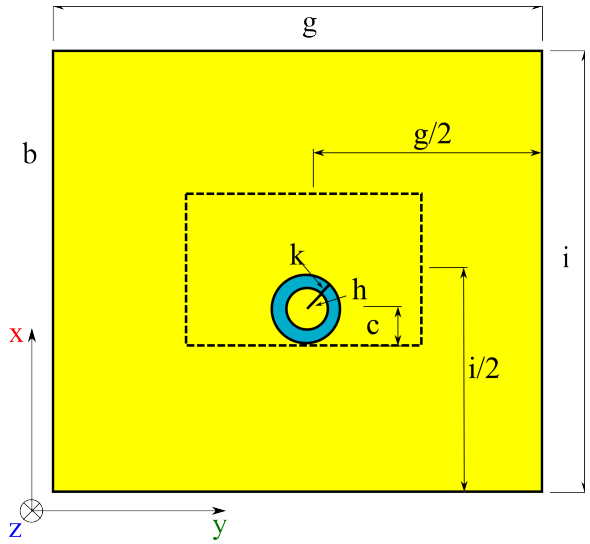

Figure 41: Bottom view of $5.8GHz$ wideband and regular rectangular patch antennas. The yellow material represents copper and the blue material represents PTFE in the coaxial feed line. The dotted line represents the rectangular patch that is on the front side of the antenna structure.

Table 6: Dimensions of the $5.8GHz$ rectangular patch antenna designed according to Figs. 37,39,40,41. All units are in mm.

Dimension	Value (mm)	Dimension	Value (mm)
a	11.78	g	40
b	16.57	h	0.6
c	2.8	i	7
d	0.25	j	40
e	0.036	k	2
f	1.5		

Table 7: Dimensions of the wideband $5.8GHz$ E-shaped rectangular patch antenna designed according to Figs. 38,39,40,41. All units are in mm.

Dimension	Value (mm)	Dimension	Value (mm)
a	29.41	h	0.6
b	10.5	i	7
c	1.1	j	50
d	0.25	k	2
e	0.036	l	4.47
f	3.7	m	2.64
g	60	n	7.65

REFERENCES

[1] Leonard B. Loeb. *Fundamental Processes of Electrical Discharge In Gasses*. John Wiley & Sons, Inc., New York, 1939.

[2] U.S. Energy Information Administration. Electric power annual 2010, 2010.

[3] Solar Energy Industries Association. U.S. solar market insight report: 2011 year-in-review. Technical report, 2011.

[4] Yi Yang, F. Lambert, and D. Divan. A survey on technologies for implementing sensor networks for power delivery systems. In *IEEE Power Engineering Society General Meeting, 2007*, pages 1–8. IEEE, June 2007.

[5] Yi Yang. *Power Line Sensor Networks for Enhancing Power Line Reliability and Utilization*. PhD thesis, Georgia Institute of Technology, Atlanta, GA, August 2011.

[6] C. R Valenta, P. A Graf, M. S Trotter, G. A Koo, G. D Durgin, and B. J Schafer. Backscatter channel measurements at 5.8 GHz across high-voltage corona. In *Sensors, 2010 IEEE*, Hilo, HI, November 2010. IEEE.

[7] R. Moghe, D. Divan, and F. Lambert. Powering low-cost utility sensors using energy harvesting. In *Proceedings of the 2011-14th European Conference on Power Electronics and Applications (EPE 2011)*, pages 1–10. IEEE, August 2011.

[8] J.D. Griffin and G.D. Durgin. Complete link budgets for backscatter-radio and RFID systems. *Antennas and Propagation Magazine, IEEE*, 51(2):11-25, 2009.

[9] Jim Lux. Corona. http://home.earthlink.net/˜jimlux/hv/corona.htm.

[10] Frederick A. Maxfield. *Theory of Gaseous Conduction of Electronics*. McGraw-Hill Book Company, Inc., New York and London, 1941.

[11] J. S Carroll and J. T Lusignan. The space charge that surrounds a conductor in corona. *American Institute of Electrical Engineers, Transactions of the*, 47(1):50–57, 1928.

[12] J. J. Clade, C. H. Gary, and C. A. Lefevre. Calculation of corona losses beyond the critical gradient in alternating voltage. *Power Apparatus and Systems, IEEE Transactions on*, (5Part-I):695-703, 2007.

[13] R. T. Waters, T. E. S. Rickard, and W. B. Stark. Direct measurement of electric field at line conductors during a.c. corona. *Proc. IEE*, 119(6):717–723, June 1972.

[14] J. M. Meek and J. D. Craggs. *Electrical Breakdown of Gases*. Clarendon Press, Oxford, 1953.

[15] C. L. Wadhwa. *High Voltage Engineering*. New Age Science, 2010.

[16] D.B. Phillips, RG Olsen, and PD Pedrow. Corona onset as a design optimization criterion for high voltage hardware. *Dielectrics and Electrical Insulation, IEEE Transactions on*, 7(6):744-751, 2000.

[17] M. Abdel-Salam and E. K Stanek. Mathematical-physical model of corona from surges on high-voltage lines. *Industry Applications, IEEE Transactions on*, (3):481-489, 2008.

[18] Patrick D. Pedrow and Robert G. Olsen. Corona streamer onset as an optimization criterion for design of high voltage hardware on transmission lines. In *Electrical Insulation, 1996., Conference Record of the 1996 IEEE International Symposium on*, volume 1, pages 312-315, 1996.

[19] A. E. Rodriguez, W. L. Morgan, K. J. Touryan, W. M. Moeny, and T. H. Martin. An air breakdown kinetic model. *Journal of Applied Physics*, 70(4):2015–2022, August 1991.

[20] T. Farouk, B. Farouk, D. Staack, A. Gutsol, and A. Fridman. Simulation of dc atmospheric pressure argon micro glow-discharge. *Plasma Sources Science and Technology*, 15:676, 2006.

[21] S. Cristina, G. Dinelli, and M. Feliziani. Numerical computation of corona space charge and VI characteristic in DC electrostatic precipitators. *Industry Applications, IEEE Transactions on*, 27(1):147–153, 1991.

[22] J. Chen and J. H Davidson. Model of the negative dc corona plasma: comparison to the positive dc corona plasma. *Plasma chemistry and plasma processing*, 23(1):83-102, 2003.

[23] J. Chen and J. H Davidson. Ozone production in the positive DC corona discharge: Model and comparison to experiments. *Plasma chemistry and plasma processing*, 22(4):495–522, 2002.

[24] Paul A. Tipler. *College Physics*. Worth Pub, 1987.

[25] F. W. Peek. *Dielectric Phenomena in High Voltage Engineering*. McGraw-Hill, New York, 1929.

[26] M. Laroussi and W. T Anderson. Attenuation of electromagnetic waves by a plasma layer at atmospheric pressure. *International journal of infrared and millimeter waves*, 19(3):453-464, 1998.

[27] M. A. Heald and C. B. Wharton. *Plasma Diagnositics With Microwaves*. Wiely, New York, 1965.

[28] S.R. Seshadri. *Fundamentals of Plasma Physics*. American Elsevier Publishing Company, Inc., New York, 1973.

[29] D. M. Dobkin and S. M. Weigand. Environmental effects on RFID tag antennas. In *Microwave Symposium Digest, 2005 IEEE MTT-S International*, page 4, 2005.

[30] C.A. Balanis. *Antenna Theory: Analysis and Design*. John Wiley & Sons, Inc., Hoboken, New Jersey, 3rd edition, 2005.

[31] L. Wei, Q. Jinghui, D. Weibo, and S. Ying. Research on an axially slotted cylinder antenna coated with plasma sheath. In *Microwave and Millimeter Wave Technology, 2008. ICMMT 2008. International Conference on*, volume 4, pages 1875-1878, 2008.

[32] Steven R. Best and Bradley C. Kaanta. A tutorial on the receiving and scattering properties of antennas. *Antennas and Propagation Magazine, IEEE*, 51(5):26-37, 2009.

[33] Fan Yang, Xue-Xia Zhang, Xiaoning Ye, and Yahya Rahmat-Samii. Wide-band e-shaped patch antennas for wireless communications. *Antennas and Propagation, IEEE Transactions on*, 49(7):1094-1100, 2001.